

Principal Components Bias in Deep Neural Networks

Guy Hacoheh

*The School of Computer Science and Engineering
Edmond and Lily Safra Center for Brain Sciences
The Hebrew University of Jerusalem
Jerusalem, Israel*

GUY.HACOHEN@MAIL.HUJI.AC.IL

Daphna Weinshall

*The School of Computer Science and Engineering
The Hebrew University of Jerusalem
Jerusalem, Israel*

DAPHNA@MAIL.HUJI.AC.IL

Abstract

Recent work suggests that convolutional neural networks of different architectures learn to classify images in the same order. To understand this phenomenon, we revisit the over-parametrized deep linear network model. Our asymptotic analysis, assuming that the hidden layers are wide enough, reveals that the convergence rate of this model's parameters is exponentially faster along directions corresponding to the larger principal components of the data, at a rate governed by the singular values. We term this convergence pattern the *Principal Components bias (PC-bias)*. We show how the *PC-bias* streamlines the order of learning of both linear and non-linear networks, more prominently at earlier stages of learning. We then compare our results to the simplicity bias, showing that both biases can be seen independently, and affect the order of learning in different ways. Finally, we discuss how the *PC-bias* may explain some benefits of early stopping and its connection to PCA, and why deep networks converge more slowly when given random labels.

Keywords: deep linear networks, learning dynamics, PC-bias, simplicity bias, learning order

1. Introduction

The dynamics of learning in deep neural networks is an intriguing subject, not yet sufficiently understood. Recent empirical studies of learning dynamics (Hacoheh et al., 2020; Pliushch et al., 2021) showed that neural networks learn the training examples of natural datasets in a consistent order, and further impose a consistent order on the test set. Below we call this effect *Learning Order Constancy (LOC)*. Currently, the characteristics of visual data, which may explain this phenomenon, remain unclear. Surprisingly, this universal order persists despite the variability introduced into the training of different models and architectures.

To understand this phenomenon, we start by analyzing the deep linear network model (Saxe et al., 2013, 2019), defined by the concatenation of linear operators. Accordingly, in Section 3 we prove that the convergence of the weights of deep linear networks is governed by the eigendecomposition of the raw data, which is blind to the labels of the data, in a phenomenon we term *PC-bias*. These asymptotic results are valid when the hidden layers are wide enough, and can be seen as an extension of the known behavior of the single-layer

convex linear model (Le Cun et al., 1991). In Section 4, we empirically show that this pattern of convergence is indeed observed in deep linear networks of moderate width, validating the plausibility of our assumptions. We continue by showing that the *LOC-effect* in deep linear networks is determined solely by their *PC-bias*. We prove a similar (weaker) result for the non-linear two-layer ReLU model introduced by Allen-Zhu et al. (2018), where this model is presented as a certain extension of NTK (Jacot et al., 2020).

In Section 5, we extend the study empirically to non-linear networks, and investigate the relationship between the *PC-bias* and the *LOC-effect* in general deep networks. We first show that the order by which examples are learned by linear networks is highly correlated with the order induced by prevalent deep CNN models. We then show directly that the learning order of non-linear CNN models is affected by the principal decomposition of the data. Moreover, the *LOC-effect* diminishes when data is whitened, indicating a tight connection between the *PC-bias* and the *LOC-effect*.

Our results are reminiscent of another phenomenon, termed *Spectral bias* (see Section 2.2), which associates the learning dynamics of neural networks with the Fourier decomposition of functions in the hypothesis space. In Section 5.3 we investigate the relation between the *PC-bias*, *spectral bias*, and the *LOC-effect*. We find that the *LOC-effect* is very robust: (i) when we neutralize the *spectral bias* by using low complexity models such as deep linear networks, the effect is still observed; (ii) when we neutralize the *PC-bias* by using whitened data, the *LOC-effect* persists. We hypothesize that at the beginning of learning, the learning dynamics of neural models is controlled by the eigendecomposition of the raw data. As learning proceeds, control of the dynamics slowly shifts to other factors.

The *PC-bias* has implications beyond the *LOC-effect*, as expanded in Section 6:

1. Early stopping. It is often observed that when training deep networks with real data, the highest generalization accuracy is obtained before convergence. Consequently, early stopping is often prescribed to improve generalization. Following the commonly used assumption that in natural images the lowest principal components correspond to noise (Torralba and Oliva, 2003), our results predict the benefits of early stopping, and relate it to PCA. In Section 6 we investigate the relevance of this conclusion to real non-linear networks (see, e.g., Basri et al. (2019); Li et al. (2020) for complementary accounts).

2. Slower convergence with random labels. Zhang et al. (2016) showed that neural networks can learn any label assignment. However, training with random label assignments is known to converge slower as compared to training with the original labels (Krueger et al., 2017). We report a similar phenomenon when training deep linear networks. Our analysis shows that when the principal eigenvectors are correlated with class identity, as is often the case in natural images, the loss decreases faster when given true label assignments as against random label assignments. In Section 6 we investigate this hypothesis empirically in linear and non-linear networks.

3. Weight initialization. Different weight initialization schemes have been proposed to stabilize the learning and minimize the hazard of "exploding gradients" (e.g., Glorot and Bengio, 2010; He et al., 2015). Our analysis (see App. §A) identifies a related variant, which eliminates the hazard when all the hidden layers are roughly of equal width. In the deep linear model, it can be proven that the proposed normalization variant in a sense minimizes repeated gradient amplification.

2. Scientific Background and Previous Work

In Section 2.1 we put our theoretical results in the context of extensive related work. In Section 2.2 we briefly discuss work on the *simplicity bias*, one expression of which being the *spectral* bias alluded to above.

2.1 Theoretical background

A large body of work concerns the analysis of deep over-parameterized linear networks. While not a universal approximator, this model is nevertheless trained by minimizing a non-convex objective function with a multitude of minima. The investigation of such networks is often employed to shed light on the learning dynamics when complex geometric landscapes are explored by GD (Fukumizu, 1998; Arora et al., 2018; Wu et al., 2019a; Du and Hu, 2019; Hu et al., 2020b; Yun et al., 2020). Note that while such networks provably achieve a simple low-rank solution (Ji and Telgarsky, 2018; Du et al., 2018) when given linearly separable data, in our work nothing like this is assumed about the data.

Early on Baldi and Hornik (1989) characterized the optimization landscape of the over-parameterized linear model and its relation to PCA. More recent work suggests that with sufficient over-parameterization, this landscape is well behaved (Kawaguchi, 2016; Zhou and Liang, 2018) and all its local minima are global (Laurent and Von Brecht, 2017). Deep linear networks are also used to study biases induced by architecture or optimization (Ji and Telgarsky, 2018; Wu et al., 2019b).

A number of related studies investigated the dynamics of learning in over-parameterized models by way of spectral analysis. However, while we employ the eigenvectors of the data covariance matrix¹ $\Sigma_{XX} = XX^\top$, most of the behavior identified in these studies is driven by the eigenvectors of the cross-covariance matrix $\Sigma_{YX} = YX^\top$. This difference is crucial, as Σ_{XX} is blind to the class labels, unlike Σ_{YX} . In addition, quite a few of the studies reviewed below assumed a shallow 2-layer network, while our analysis accommodates over-parametrized networks of any depth, further showing that convergence depends on the eigenvectors of Σ_{XX} rather than Σ_{YX} without any additional assumption.

More specifically, Saxe et al. (2019) analyzed the evolution of learning dynamics in a shallow 2-layers linear model, showing that convergence is guided by the eigenvectors of Σ_{YX} . This analysis assumed $\Sigma_{XX} = I_d$, thus obscuring the dependence of convergence on the raw data eigenvectors of Σ_{XX} , as all the eigenvalues are now identical by assumption. Likewise, Arora et al. (2018) also assume that $\Sigma_{XX} = I_d$ while investigating continuous gradients of the deep linear model and allowing for a more general loss. Although there is some superficial resemblance between their pre-conditioning and our *gradient scale matrices* as defined below, they are defined quite differently and have different properties.

Similarly to Saxe et al. (2019), Gidel et al. (2019) also investigated a shallow 2-layers linear model, but no longer assumed that $\Sigma_{XX} = I_d$. Instead, they assumed that Σ_{XX} and Σ_{YX} can be jointly decomposed, having the same eigenvectors. Under these conditions they were able to show that convergence is guided by the eigenvectors of Σ_{YX} , which correspond to the eigenvectors of Σ_{XX} by the joint decomposition assumption. However, Σ_{XX} in this case still depends on the class labels by assumption, which is not realistic for many datasets.

1. X and Y denote the matrices whose columns are the data points and one-hot label vectors respectively, see notations in Section 3.

Recently, Nguyen (2021) showed that the learning dynamics of 2 layers non-linear auto-encoders converge faster along the eigenvectors of Σ_{XX} . While their results resemble ours, unlike us they focus on auto-encoders and assume that the data is sampled from a Gaussian distribution.

Another line of related work was pioneered by Jacot et al. (2020), who showed how neural networks can be analyzed using kernel theory and introduced the Neural Tangent Kernel (NTK). In this framework, it has been shown that convergence is fastest along the largest **kernel's** principal components. In the one-layer linear model, this result implies that convergence depends on the eigenvectors of Σ_{XX} , but to the best of our knowledge, it was not extended to the over-parameterized deep model analyzed here. While similar results to ours may be achieved in the future by using kernel theory, we provide here direct proof, thus bypassing possible limitations of this kernel theory (Chizat et al., 2018; Yehudai and Shamir, 2019). This direct proof further enables us to examine the behavior outside the limit of infinite width, and carefully examine our assumptions using empirical methods.

2.2 Simplicity Bias

Diverse empirical observations seem to support the hypothesis that neural networks start by learning a simple model, which then gains complexity as learning proceeds (Gunasekar et al., 2018; Soudry et al., 2018; Hu et al., 2020a; Nakkiran et al., 2019; Gissin et al., 2019; Heckel and Soltanolkotabi, 2019; Ulyanov et al., 2018; Valle-Perez et al., 2018). This phenomenon is sometimes called *simplicity bias* (Dingle et al., 2018; Shah et al., 2020).

In a related line of work, Rahaman et al. (2019) empirically demonstrated that the complexity of classifiers learned by ReLU networks increases with time. Basri et al. (2019, 2020) showed theoretically, by way of analyzing elementary neural network models, that these models first fit the data with low-frequency functions, and gradually add higher frequencies to improve the fit. Nevertheless, the *spectral bias* and *PC-bias* are inherently different. Indeed, the eigendecomposition of raw images is closely related to the Fourier analysis of images as long as the statistical properties of images are (approximately) translation-invariant (Simoncelli and Olshausen, 2001; Torralba and Oliva, 2003). Still, the *PC-bias* is guided by spectral properties of the raw data and is therefore blind to class labels. On the other hand, the *spectral bias*, as well as the related *frequency bias* that has been shown to characterize NTK models (Basri et al., 2020), are all guided by spectral properties of the learned hypothesis, which crucially depend on label assignment.

3. Theoretical analysis

Notations. Let $\mathbb{X} = \{(\mathbf{x}_i, \mathbf{y}_i)\}_{i=1}^n$ denote the training data, where $\mathbf{x} \in \mathbb{R}^q$ denotes the i -th data point and $\mathbf{y} \in \{0, 1\}^K$ its corresponding label. Let $\frac{1}{n_i} \mathbf{m}_i$ denote the centroid (mean) of class i with n_i points, and $M = [\mathbf{m}_1 \dots \mathbf{m}_K]^\top$. Finally, let X and Y denote the matrices whose i^{th} column is \mathbf{x}_i and \mathbf{y}_i respectively. $\Sigma_{XX} = XX^\top$ and $\Sigma_{YX} = YX^\top$ denote the covariance matrix of X and cross-covariance of X and Y respectively. We note that Σ_{XX} captures the structure of the data irrespective of class identity.

Definition 1 (Principal coordinate system) *The coordinate system obtained by rotating the data in \mathbb{R}^q by an orthonormal matrix U^\top , where $SVD(\Sigma_{XX}) = UDU^\top$. Now $\Sigma_{XX} = D$,*

a diagonal matrix whose elements are the singular values of XX^\top , arranged in decreasing order $d_1 \geq d_2 \geq \dots \geq d_q \geq 0$.

Definition 2 (Compact representation) Let $f(\mathbf{x})$ denote a deep linear network. Then $f(\mathbf{x}) = \left(\prod_{l=L}^1 W_l \right) \mathbf{x} = \mathbf{W} \mathbf{x}$, where $\mathbf{W} \in \mathbb{R}^{K \times q}$ is called the compact representation of the network.

Definition 3 (Error matrix) For a deep linear network whose compact representation is \mathbf{W} , the error matrix is $Er = \mathbf{W} \Sigma_{XX} - \Sigma_{YX}$. In the principal coordinate system, $Er = \mathbf{W} D - M$.

Assumptions. Our analysis assumes that the learning rate μ is infinitesimal, and therefore terms of size $O(\mu^2)$ can be neglected. We further assume that the width of the hidden layers lies in $[\mathfrak{m}, \mathfrak{m} + M_b]$, where $\mathfrak{m} \rightarrow \infty$ denotes a very large number and M_b is fixed. Thus terms of size $O(\frac{1}{\mathfrak{m}})$ can also be neglected. In Fig. 1 we show the plausibility of these assumptions, where the predicted dynamics is seen throughout the training of deep linear networks, even for small values of \mathfrak{m} .

3.1 The dynamics of deep over-parametrized linear networks

Consider a deep linear network with L layers, and let

$$L(\mathbb{X}) = \frac{1}{2} \|\mathbf{W} X - Y\|_F^2 \quad \mathbf{W} := \prod_{l=L}^1 W_l, \quad W_l \in \mathbb{R}^{m_l \times m_{l-1}} \quad (1)$$

Above m_l denotes the number of neurons in layer l , where $m_0 = q$ and $m_L = K$. Extending the analysis described in Du and Hu (2019); Du et al. (2019), we derive the temporal dynamics of \mathbf{W} :

Proposition 4 In each time point s , the compact matrix representation \mathbf{W} obeys the following dynamics, when using the notation Er^s defined in Def. 3:

$$\mathbf{W}^{s+1} = \mathbf{W}^s - \mu \sum_{l=1}^L A_l^s \cdot Er^s \cdot B_l^s + O(\mu^2) \quad (2)$$

Above μ denotes the learning rate. A_l^s and B_l^s are called gradient scale matrices, and are defined as

$$A_l^s := \left(\prod_{j=L}^{l+1} W_j^s \right) \left(\prod_{j=L}^{l+1} W_j^s \right)^\top \in \mathbb{R}^{K \times K} \quad B_l^s := \left(\prod_{j=l-1}^1 W_j^s \right)^\top \left(\prod_{j=l-1}^1 W_j^s \right) \in \mathbb{R}^{q \times q} \quad (3)$$

The proof can be found in Appendix §B.

Gradient scale matrices. Some statistical properties of such matrices are established in Appendix §A. Note that when the number of hidden layers is 0 ($L = 1$), both gradient scale matrices reduce to the identity matrix and the dynamics in (2) is reduced to the following known result (e.g., Le Cun et al., 1991): $\mathbf{W}^{s+1} = \mathbf{W}^s - \mu E r^s$. Recall, however, that the focus of this paper is the over-parameterized linear model with $L > 1$, in which the loss is not convex. Since the difference between the convex linear model and the over-parametrized deep model boils down to these matrices, our convergence analysis henceforth focuses on the dynamics of the *gradient scale matrices*.

In accordance, we analyze the evolution of the *gradient scale matrices* as learning proceeds. Let $\mathfrak{m} = \min(m_1, \dots, m_{L-1})$ denote the size of the smallest hidden layer. Initially for $s = 0$, all weight matrices W_l^0 are assumed to be initialized by sampling from a distribution with mean 0 and variance $\sigma_l^2 = O(\frac{1}{\mathfrak{m}})$. The specific normalization factor, alluded to in $O(\frac{1}{\mathfrak{m}})$, is a variant of the Glorot initialization. Details and justification can be found in Appendix §A.1.

At time s , let $A_l^s(\mathfrak{m})$ and $B_l^s(\mathfrak{m})$ denote a sequence of random *gradient scale matrices*, corresponding to networks whose smallest hidden layer has \mathfrak{m} neurons. From Appendix §A we deduce that:

Theorem 5 Using \xrightarrow{p} to denote convergence in probability as $\mathfrak{m} \rightarrow \infty$, and $\forall s, l$:

$$B_l^s(\mathfrak{m}) \xrightarrow{p} I, \quad \text{var}[B_l^s(\mathfrak{m})] = O\left(\frac{1}{\mathfrak{m}}\right) \quad A_l^s(\mathfrak{m}) \xrightarrow{p} I, \quad \text{var}[A_l^s(\mathfrak{m})] = O\left(\frac{1}{\mathfrak{m}}\right)$$

Proof Proof by induction on s . Initially when $s = 0$, the claim follows from Thm 12 and Corr 14. The induction step validity follows from Thm 15 and Thm 16 (see Appendix §A.2). ■

The detailed proof shows that the relevant constants are amplified with s . While they remain moderate and \mathfrak{m} is sufficiently large, $B_l^s(\mathfrak{m}) \approx I$ and $A_l^s(\mathfrak{m}) \approx I \forall l$. In this case, the dynamics of the over-parameterized model is identical to the dynamics of the convex linear model, $\mathbf{W}^{s+1} = \mathbf{W}^s - \mu E r^s$.

Convergence rate. In §A.2 we show that the convergence of $B_l^s(\mathfrak{m})$ to I is governed to some extent by $O(\frac{K}{\mathfrak{m}})$, while the convergence of $A_l^s(\mathfrak{m})$ is governed by $O(\frac{q}{\mathfrak{m}})$. Recall that while $\mathfrak{m} \rightarrow \infty$, q is the dimension of the data space which is fixed in advance and can be fairly large, while K is the number of classes which is fixed and quite small. Typically, $K \ll q$. Thus we expect the right *gradient scale matrices* $B_l^s(\mathfrak{m})$ to remain approximately I much longer than the left matrices $A_l^s(\mathfrak{m})$.

Empirical validation. Since the results above are asymptotic, and to envision the difference between convergence governed by $O(\frac{K}{\mathfrak{m}})$ vs. $O(\frac{q}{\mathfrak{m}})$, we resort to simulations whose results are shown in Fig. 1. These empirical results, recounting linear networks with 4 hidden layers of width 1024, clearly show that during a significant part of the training both *gradient scale matrices* remain approximately I . The difference between the convergence rate of B_l^s and A_l^s is seen later on, when ΔA_l^s starts to increase shortly before convergence, while ΔB_l^s remains essentially 0 throughout.

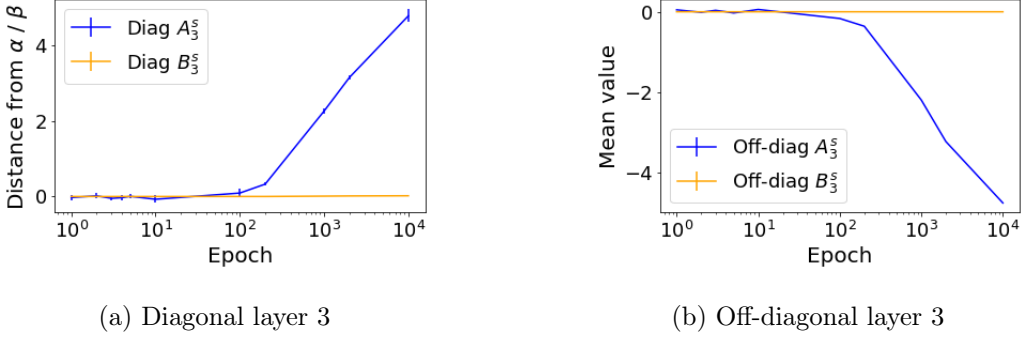


Figure 1: The dynamics of A_l^s and B_l^s when training 10 5-layered linear networks on the small-mammals dataset. (a) Mean distance of the diagonal elements of A_l^s and B_l^s from α_i^s and β_i^s (as defined in Thm 9, §A.1). (b) Mean value of the off-diagonal elements of A_l^s and B_l^s . The networks reach maximal test accuracy at epoch $s = 100$, before the divergence of A_l^s . All layers behave similarly.

3.2 Weight evolution

$K \ll q$ entails that $B_l^s(\mathbf{m})$ remains approximately equal to I much longer than $A_l^s(\mathbf{m})$. This is substantiated by the simulation results in Fig. 1. Consequently, at the beginning the assumption that both $A_l^s \approx I$ and $B_l^s \approx I$ is justified, but as learning proceeds, we can only safely assume that $B_l^s \approx I$.

With this in mind, we obtain expressions for the evolution of \mathbf{W}^s separately for earlier and later stages of learning. We first shift to the principal coordinate system defined in Def 1. In this system, we can analyze each column of \mathbf{W}^s separately, where \mathbf{w}_j^s and \mathbf{m}_j denote the respective columns of \mathbf{W}^s and M .

Theorem 6 *At the beginning of learning when both $A_l^s \approx I$ and $B_l^s \approx I$:*

$$\mathbf{w}_j^{s+1} = (\lambda_j)^s \mathbf{w}_j^0 + [1 - (\lambda_j)^s] \frac{\mathbf{m}_j}{d_j} = (\lambda_j)^s \mathbf{w}_j^0 + [1 - (\lambda_j)^s] \mathbf{w}_j^{opt} \quad \lambda_j = 1 - \mu d_j L \quad (4)$$

See App. B.1 for complete proof. Thm 6 is reminiscent of the well-understood dynamics of training the convex one-layer linear model. It is composed of two additive terms, revealing two parallel and independent processes:

1. The dependence on random initialization tends to 0 exponentially with decline rate λ_j .
2. The final value is the sum of a geometrical series with a common ratio λ_j .

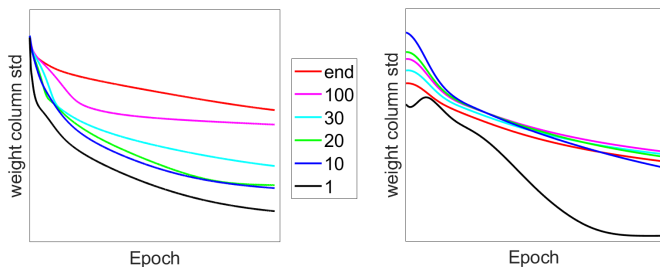
In either case, convergence is fastest for the largest singular eigenvalue, or the first column of \mathbf{W} , and slowest for the smallest singular value. This behavior is visualized in Fig. 2a. Importantly, the rate of convergence depends on the singular value d_j , the number of layers L , and the learning rate μ .

Theorem 7 *In later stages of learning, when we can only assume that $B_l^s \approx I$:*

$$\mathbf{w}_j^{s+1} = \prod_{\nu=1}^s (I - \mu d_j A^\nu) \mathbf{w}_j^0 + \mu \left[\sum_{\nu=1}^s \prod_{\rho=\nu+1}^s (I - \mu d_j A^\rho) A^\nu \right] \mathbf{m}_j \quad (5)$$

where $A^s = \sum_{l=1}^L A_l^s$.

The proof is provided in App. B.1. Although the dynamics now depends on matrices A^s as well, it is still the case that the convergence of each column is governed by its singular value d_j . This suggests that while the *PC-bias* is more pronounced in earlier stages of learning, its effect persists throughout.



(a) 2-layer linear network (b) 2-layer ReLU network

Figure 2: Empirical confirmation of the theoretical results reported below, showing the std of \mathbf{w}_j over 10 independently trained networks as a function of the epoch, for 6 specific principal components (see legend).

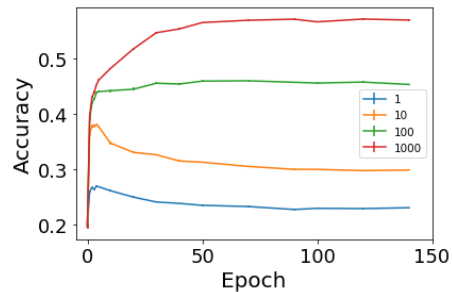


Figure 3: Mean accuracy of 10 st-VGG networks evaluated on test data projected to dimensionality $\{1, 10, 100, 1000\}$.

3.3 Adding Non-Linear ReLU Activation

We extend the results above to a relatively simple non-linear model suggested and analyzed by Allen-Zhu et al. (2018); Arora et al. (2019); Basri et al. (2019), here adapted to classification rather than regression. Specifically, it is a two-layer model with ReLU activation, where only the weights of the first layer are being learned. Similarly to (1), the loss is defined as

$$L(\mathbb{X}) = \frac{1}{2} \sum_{i=1}^n \|f(\mathbf{x}_i) - \mathbf{y}_i\|^2 \quad f(\mathbf{x}_i) = \mathbf{a}^\top \cdot \sigma(W \mathbf{x}_i), \quad \mathbf{a} \in \mathbb{R}^m, \quad W \in \mathbb{R}^{m \times d}$$

m denotes the number of neurons in the hidden layer. We consider a binary classification problem with 2 classes, where $y_i = 1$ for $\mathbf{x}_i \in C_1$, and $y_i = -1$ for $\mathbf{x}_i \in C_2$. $\sigma(\cdot)$ denotes the ReLU activation function $\sigma(u) = \max(u, 0)$. Unlike deep linear networks, the analysis in this case require additional two strong symmetry assumptions:

1. The distribution of the data is symmetric: $P(\mathbf{x}_i) = P(-\mathbf{x}_i)$.
2. W and \mathbf{a} are initialized symmetrically so that $\mathbf{w}_{2i}^0 = -\mathbf{w}_{2i-1}^0$ and $a_{2i} = -a_{2i-1} \quad \forall i \in [\frac{m}{2}]$.

Theorem 8 *Under the assumptions above, at the beginning of the learning, the temporal dynamics of the models can be shown to obey the following update rule:*

$$W^{s+1} \approx W^s - \mu \frac{1}{2} [(\mathbf{a}\mathbf{a}^\top)W^s \Sigma_{XX} - \tilde{M}^s]$$

Above \tilde{M}^s denotes the difference between the centroids of the 2 classes, computed in the half-space defined by $\mathbf{w}_r^s \cdot \mathbf{x} \geq 0$.

The complete proof can be found in App. B.3. Thm 8 is reminiscent of the single-layer linear model dynamics $\mathbf{W}^{s+1} = \mathbf{W}^s - \mu E r^s$, and we may conclude that when it holds and using the principal coordinate system, the rate of convergence of the j -th column of W^s is governed by the singular value d_j . In Fig. 2b, we confirm these results empirically, demonstrating the convergence of weights of 10 ReLU models trained on the small mammals (see App. D.4) dataset, along different principal directions of the data.

4. PC-bias: empirical study

In this section, we first analyze deep linear networks, showing that the convergence rate is indeed governed by the principal singular values of the data, which demonstrates the plausibility of the assumptions made in Section 3. We continue by extending the scope of the investigation to non-linear neural networks, finding evidence for the *PC-bias* mostly in the earlier stages of learning.

4.1 Methodology

We say that a linear network is L -layered when it has $L - 1$ hidden fully connected (FC) layers (without convolutional layers). In our empirical study, we relaxed some assumptions of the theoretical study, to increase the resemblance of the trained networks to networks in common use. Specifically, we changed the initialization to the commonly used Glorot initialization, replaced the L_2 loss with the cross-entropy loss, and employed SGD instead of the deterministic GD. Notably, the original assumptions yielded similar results. The results presented summarize experiments with networks of equal width across all hidden layers, specifically the moderate² value of $m = 1024$, keeping in mind that we test the relevance of asymptotic results for $m \rightarrow \infty$. Using a different width for each layer yielded similar qualitative results. Details regarding the hyper-parameters, architectures, and datasets can be found in §D.1, §D.3 and §D.4 respectively.

4.2 PC-bias in deep linear networks

In this section, we train L -layered linear networks, then compute their compact representations \mathbf{W} rotated to align with the canonical coordinate system (Def. 1). Note that each row \mathbf{w}_r in \mathbf{W} essentially defines the one-vs-all separating hyper-plane corresponding to class r .

To examine both the variability between models and their convergence rate, we inspect \mathbf{w}_r at different time points during learning. The rate of convergence can be measured directly, by

2. Note that for most image datasets, q (the input dimension) is much larger than 1024, and therefore $\frac{q}{m} \gg 1$. In this sense $m = 1024$ is moderate, as one can no longer assume $A_l^s(m) \approx I$.

observing the changes in the weights of each element in \mathbf{w}_r . These weight values³ should be compared with the optimal values in each row \mathbf{w}_r of $W_{opt} = YX^T(XX^T)^{-1}$. The variability between models is measured by calculating the standard deviation (std) of each \mathbf{w}_r across N models.

We begin with linear networks. We trained 10 5-layered FC linear networks, and 10 linear st-VGG convolutional networks. When analyzing the compact representation of such networks we observe a similar behavior – weights corresponding to larger principal components converge faster to the optimal value, and their variability across models converges faster to 0 (Figs. 4a,4b). Thus, while the theoretical results are asymptotic, *PC-bias* is empirically seen throughout the entire learning process of deep linear networks.

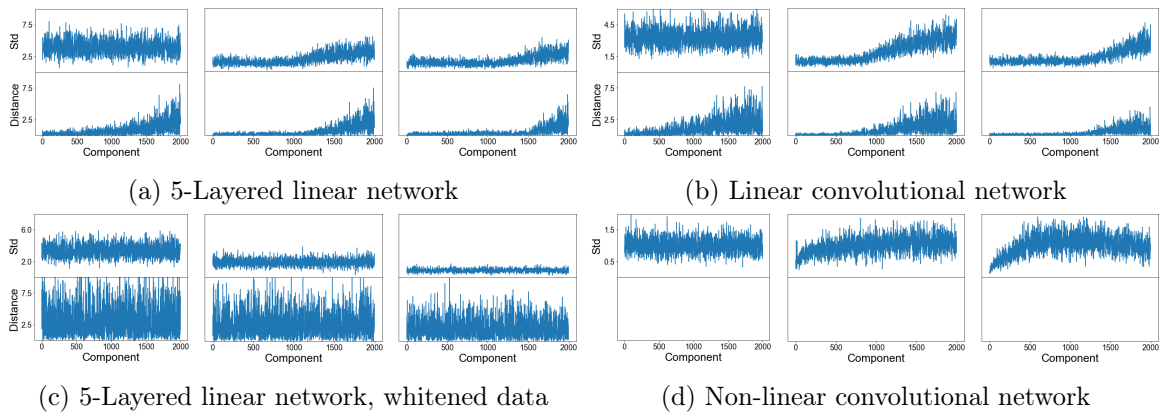


Figure 4: Convergence of the compact representation along the principal directions in different epochs. The value of the X -axis corresponds to the index of a principal eigenvalue, from the most significant to the least significant. (a) 10 5-layered linear networks trained on the cats and dogs dataset. 3 plots are provided, corresponding to snapshots taken at different stages of learning: the beginning (epoch 0, left), intermediate stage (middle), and close to convergence (right). Bottom panel: average distance of the weights in \mathbf{w}_1 from the optimal linear classifier; top panel: respective std. (b) Similarly, for 10 linear st-VGG convolutional networks, trained on CIFAR-10. (c) Similarly, for 10 5-layered linear networks, trained on the cats and dogs dataset, with ZCA-whitening. (d) Similarly, for 10 **non-linear** st-VGG networks trained on the cats and dogs dataset. Here the distance to the optimal solution is not well defined and we therefore only show the std.

Whitened data. The *PC-bias* is neutralized when the data is whitened, at which point Σ_{XX} is the scaled identity matrix. In Fig. 4c, we plot the results of the same experimental protocol while using a ZCA-whitened dataset. As predicted, the networks no longer show any bias towards any principal direction. Weights in all directions are scaled similarly, and the std over all models is the same in each epoch, irrespective of the principal direction. (Additional experiments show that this is *not* an artifact of the lack of uniqueness when deriving the principal components of a white signal).

3. We note that the weights tend to start larger for smaller principal components, see Fig. 4a left.

4.3 PC-bias in general CNNs

In this section, we investigate the manifestation of the *PC-bias* in non-linear deep convolutional networks. As we cannot directly track the learning dynamics separately in each principal direction of non-linear networks, we adopt two different evaluation mechanisms:

Linear approximation. We considered several linear approximations, but since all of them showed the same qualitative behavior, we report results with the simplest one. Specifically, to obtain a linear approximation of a non-linear network, without max-pooling or batch-normalization layers, we follow the definition of the compact representation from Section 3 while ignoring any non-linear activation. We then align this matrix with the canonical coordinate system (Def. 1), and observe the evolution of the weights and their std across models along the principal directions during learning. Note that now the networks do not converge to the same compact representation, which is not unique. Nevertheless, we see that the *PC-bias* governs the weight dynamics to a noticeable extent.

More specifically, in these networks, a large fraction of the lowest principal components hardly changes during learning, as good as being ignored. Nevertheless, the *PC-bias* affects the higher principal components, most notably at the beginning of training (see Fig. 4d). Thus weights corresponding to higher principal components converge faster, and the std across models of such weights decreases faster for higher principal components.

Projection to higher PC's. We created a modified *test-set*, by projecting each test example on the span of the first P principal components. This is equivalent to reducing the dimensionality of the test set to P using PCA. We trained an ensemble of $N=100$ st-VGG networks on the original small mammals training set, then evaluated these networks during training on 4 versions of the test-set, reduced to $P=1,10,100,1000$ dimensions respectively. Mean accuracy is plotted in Fig. 3. Similar results are obtained when training VGG-19 (Simonyan and Zisserman, 2014) networks on CIFAR-10 (Krizhevsky et al., 2009), see §C.3.

Taking a closer look at Fig. 3, we see that when evaluated on lower dimensionality test-data ($P=1,10$), the networks' accuracy peaks after a few epochs, at which point performance starts to decrease. This result suggests that the networks rely more heavily on these dimensions in the earlier phases of learning, and then continue to learn other things. In contrast, when evaluated on higher dimensionality test-data ($P=100,1000$), accuracy continues to rise, longer so for larger P . This suggests that significant learning of the additional dimensions continues in later stages of the learning.

5. PC-bias: Learning Order Constancy

In this section, we show that the *PC-bias* is significantly correlated with the learning order of deep neural networks, and can therefore partially account for the *LOC-effect* described in Section 1. Following Hacoen et al. (2020), we measure the "speed of learning" of each example by computing its *accessibility* score. This score is computed per example, and characterizes how fast an ensemble of N networks learns it. Formally, $accessibility(\mathbf{x}) = \mathbb{E}[\mathbb{1}(f_i^e(\mathbf{x}) = y(\mathbf{x}))]$, where $f_i^e(\mathbf{x})$ denotes the outcome of the i -th network trained over e epochs, and the mean is taken over networks and epochs. For the set of datapoints

$\{(\mathbf{x}_j, \mathbf{y}_j)\}_{j=1}^n$, *Learning Order Constancy* is manifested by the high correlation between 2 instances of *accessibility*(\mathbf{x}), each computed from a different ensemble.

PC-bias is shown to pertain to *LOC* in two ways: First, in Section 5.1 we show a high correlation between the learning order in deep linear and non-linear networks. Since the *PC-bias* fully accounts for *LOC* in deep linear networks, this suggests it also accounts (at least partially) for the observed *LOC* in non-linear networks. Comparison with the *critical principal component* verifies this assertion. Second, we show in Section 5.2 that when the *PC-bias* is neutralized, *LOC* diminishes as well. In Section 5.3 we discuss the relationship between the *spectral bias*, *PC-bias* and the *LOC-effect*.

5.1 PC-Bias is correlated with LOC

We first compare the order of learning of non-linear models and deep linear networks by computing the correlation between the *accessibility* scores of both models. This comparison reveals high correlation ($r = 0.85$, $p < 10^{-45}$), as seen in Fig. 5a. To investigate directly the connection between the *PC-bias* and *LOC*, we define the *critical principal component* of an example to be the first principal component P , such that a linear classifier trained on the original data can classify the example correctly when projected to P principal components. We trained $N=100$ st-VGG networks on the cats and dogs dataset, and computed for each example its *accessibility* score and *critical principal component*. In Fig. 5b we see strong negative correlation between the two scores ($p=-0.93$, $r < 10^{-4}$), suggesting that the *PC-bias* affects the order of learning as measured by *accessibility*.

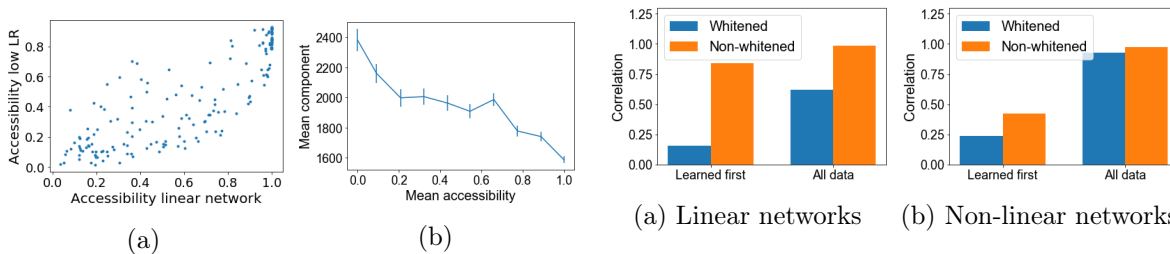


Figure 5: (a) Correlation between the *accessibility* score of $N=100$ st-VGG networks trained with a low learning rate⁴, and $N=100$ linear st-VGG networks, trained on small mammals. (b) Correlation between the accessibility score of $N=100$ st-VGG networks trained on cats and dogs, and the *critical principal component* score. The *accessibility* plot is smoothed by moving average of width 10. Error bars indicate standard error.

Figure 6: *LOC* measured with and without *PC-bias*. Each bar represents the correlation between the learning order of 2 collections of 10 networks trained on CIFAR-10. Orange bars represent natural images, in which the *PC-bias* is present, while blue bars represent whitened data, in which the *PC-bias* is eliminated. As *PC-bias* is more prominent earlier on, we compare these correlations for the entire data (right 2 bars), and for the subset of 20% "fastest learned" examples (left 2 bars).

4. As non-linear models achieve the accuracy of linear models within an epoch or 2, a low learning rate is used.

5.2 Neutralizing the PC-bias leads to diminishing LOC

Whitening the data eliminates the *PC-bias* as shown in Fig. 4c, since all the singular values are now identical. Here we use this observation to further probe into the dependency of the *Learning Order Constancy* on the *PC-bias*. Starting with the linear case, we train 4 ensembles of $N=10$ 2-layered linear networks on the cats and dogs dataset, 2 with and 2 without ZCA-whitening. We compute the *accessibility* score for each ensemble separately, and correlate the scores of the 2 ensembles in each test case. Each correlation captures the consistency of the *LOC-effect* for the respective condition. This correlation is expected to be very high for natural images. Low correlation implies that the *LOC-effect* is weak, as training the same network multiple times yields a different learning order.

Fig. 6a shows the results for deep linear networks. As expected, the correlation when using natural images is very high. However, when using whitened images, correlation plummets, indicating that the *LOC-effect* is highly dependent on the *PC-bias*. We note that the drop in the correlation is much higher when considering only the 20% "fastest learned" examples, suggesting that the *PC-bias* affects learning order more evidently at earlier stages of learning.

Fig. 6b shows the results when repeating this experiment with non-linear networks, training 2 collections of $N=10$ VGG-19 networks on CIFAR-10. We find that the elimination of the *PC-bias* in this case affects *LOC* much less, suggesting that the *PC-bias* can only partially account for the *LOC-effect* in the non-linear case. However, we note that at the beginning of learning, when the *PC-bias* is most pronounced, once again the drop is much larger and very significant (half).

5.3 Spectral bias, PC-bias and LOC

The *spectral bias* (Rahaman et al., 2019) characterizes the dynamics of learning in neural networks differently, asserting that initially neural models can be described by low frequencies only. This may provide an alternative explanation to LOC. Recall that LOC is manifested in the consistency of the *accessibility* score across networks. To compare between the *spectral bias* and *accessibility* score, we first need to estimate for each example whether it can be correctly classified by a low frequency model. Accordingly, we define for each example a *discriminability* measure – the percentage out of its k neighbors that share with it class identity. Intuitively, an example has a low *discriminability* score when it is surrounded by examples from other classes, which forces the learned boundary to incorporate high frequencies. In §C.2 we show that in the 2D case analyzed by Rahaman et al. (2019), this measure strongly correlates ($r=-0.8$, $p < 10^{-2}$) with the spectral bias.

We trained several networks (VGG-19 and st-VGG) on several real datasets, including small-mammals, STL-10, CIFAR-10/100 and a subset of ImageNet-20 (Russakovsky et al., 2015). For each network and dataset, we computed the *accessibility* score as well as the *discriminability* of each example. The vector space, in which discriminability is evaluated, is either the raw data or the network’s perceptual space (penultimate layer activation). The correlation between these scores is shown in Table 1.

Using raw data, low correlation is still seen between the *accessibility* and *discriminability* scores when inspecting the smaller datasets (small mammals, CIFAR-100 and STL10). This correlation vanishes when considering the larger ImageNet-20 dataset. It would appear that on its own, the *spectral bias* cannot adequately explain the *LOC-effect*. On the other hand,

Table 1: Correlation between *accessibility* and *discriminability*.

Dataset	Raw data	Penultimate
Small mammals	0.46	0.85
ImageNet 20	0.01	0.54
CIFAR-100	0.51	0.85
STL10	0.44	0.7

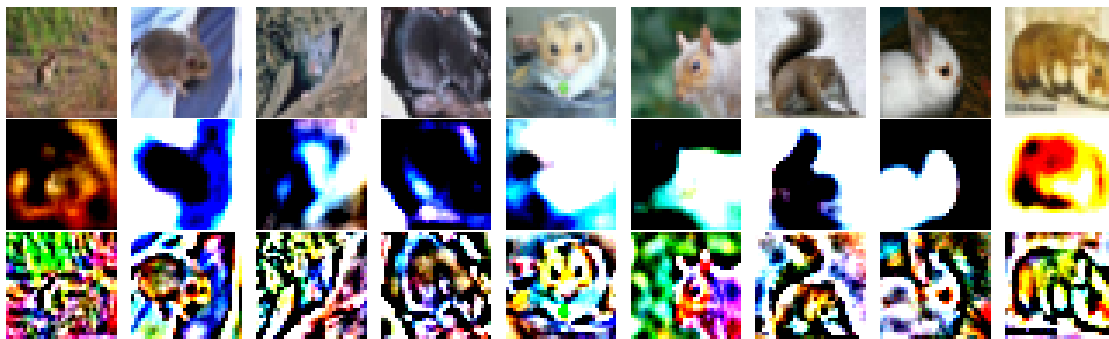


Figure 7: Visualization of the small mammals dataset, with amplification of 1.5% of its principal components by a factor of 10. Top: original data; middle: data amplified along the first principal components; bottom: data amplified along the last principal components

in the perceptual space, the correlation between *discriminability* and *accessibility* is quite significant for all datasets. Contrary to our supposition, it seems that networks learn a representation where the *spectral bias* is evident, but this bias does not necessarily govern its learning before the representation has been learned.

6. PC-bias: further implications

Early Stopping and the Generalization Gap. Considering natural images, it is often assumed that the least significant principal components of the data represent noise (Torralba and Oliva, 2003). In such cases, our analysis predicts that as noise dominates the components learned later in learning, early stopping is likely to be beneficial. To test this hypothesis directly, we manipulated CIFAR-10 to amplify the signal in either the 1.5% most significant (higher) or 1.5% least significant (lower) principal components (see examples in Fig. 7). Accuracy over the original test set, after training 10 st-VGG and linear st-VGG networks on these manipulated images, can be seen in Fig. 8. Both in linear and non-linear networks, early stopping is more beneficial when lower principal components are amplified, and significantly less so when higher components are amplified, as predicted by the *PC-bias*.

Slower Convergence with Random Labels. Deep neural models can learn any random label assignment to a given training set (Zhang et al., 2016). However, when trained on

randomly labeled data, convergence appears to be much slower (Krueger et al., 2017). Assume, as before, that in natural images the lower principal components are dominated by noise. We argue that the *PC-bias* now predicts this empirical result, since learning randomly labeled examples requires signal present in lower principal components. To test this hypothesis directly, we trained 10 2-layered linear networks on datasets of natural images. Indeed, these networks converge slower with random labels (see Fig. 9a). In Fig. 9b we repeat this experiment after having whitened the images, to neutralize the *PC-bias*. Now convergence rate is identical, whether the labels are original or shuffled. Clearly, in deep linear networks, the *PC-bias* gives a full account of this phenomenon.

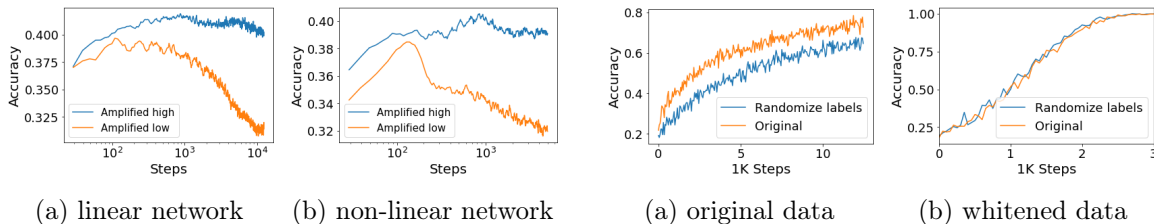


Figure 8: Effects of amplifying the highest (blue) and lowest (orange) principal components.

Figure 9: Learning curves of 10 2-layered linear networks, with real and shuffled labels, (a) before and (b) after whitening.

To further check the relevance of this account to non-linear networks, we artificially generate datasets where only the first P principal components are discriminative, while the remaining components become noise by design. We constructed two such datasets: in one the labels are correlated with the original labels, in the other they are not. Specifically, PCA is used to reduce the dimensionality of a two-class dataset to P , and the optimal linear separator in the reduced representation is computed. Next, all the labels of points that are incorrectly classified by the optimal linear separator are switched, so that the train and test sets are linearly separable by this separator. Note that the modified labels are still highly correlated with the original labels (for $P = 500$: $p = 0.82$, $r < 10^{-10}$). The second dataset is generated by repeating the process while starting from randomly shuffled labels. This dataset is likewise fully separable when projected to the first P components, but its labels are uncorrelated with the original labels (for $P = 500$: $p = 0.06$, $r < 10^{-10}$).

The mean training accuracy of 10 non-linear networks with $P=10,50,500$ is plotted in Fig. 10a (first dataset) and Fig. 10b (second dataset). In both cases, the lower P is (namely, only the first few principal components are discriminative), the faster the data is learned by the non-linear network. Whether the labels are real or shuffled makes little qualitative difference, as predicted by the *PC-bias*.

7. Summary and discussion

When trained with gradient descent, the convergence rate of the over-parameterized deep linear network model is provably governed by the eigendecomposition of the data, and specifically, parameters corresponding to the most significant principal components converge faster than the least significant components. Empirical evidence is provided for the relevance of these results to more realistic non-linear networks. We term this effect *PC-bias*. This

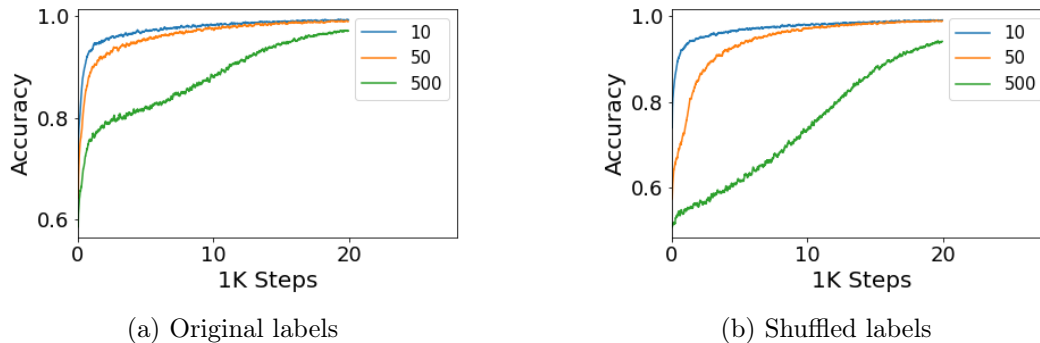


Figure 10: Learning curves of st-VGG networks trained on 3 datasets, which are linearly separable after projection to the highest P principal components (see legend).

result provides a complementary account for some prevalent empirical observations, including the benefit of early stopping and the slower convergence rate with shuffled labels.

We use the *PC-bias* to explicate the *Learning Order Constancy (LOC)*, showing that examples learned at earlier stages are more distinguishable by the higher principal components, demonstrating that networks’ training relies more heavily on higher principal components early on. A causal link between the *PC-bias* and the *LOC-effect* is demonstrated, as the *LOC-effect* diminishes when the *PC-bias* is eliminated by whitening the images. We analyze these findings given a related phenomenon termed *spectral bias*. While the *PC-bias* may be more prominent early on, the *spectral bias* may be more important in later stages of learning.

References

- Zeyuan Allen-Zhu, Yuanzhi Li, and Yingyu Liang. Learning and generalization in overparameterized neural networks, going beyond two layers. *arXiv preprint arXiv:1811.04918*, 2018.
- Sanjeev Arora, Nadav Cohen, and Elad Hazan. On the optimization of deep networks: Implicit acceleration by overparameterization. In *International Conference on Machine Learning*, pages 244–253, 2018.
- Sanjeev Arora, Simon Du, Wei Hu, Zhiyuan Li, and Ruosong Wang. Fine-grained analysis of optimization and generalization for overparameterized two-layer neural networks. In *International Conference on Machine Learning*, pages 322–332, 2019.
- Pierre Baldi and Kurt Hornik. Neural networks and principal component analysis: Learning from examples without local minima. *Neural networks*, 2(1):53–58, 1989.
- Ronen Basri, David W. Jacobs, Yoni Kasten, and Shira Kritchman. The convergence rate of neural networks for learned functions of different frequencies. In *Advances in Neural Information Processing Systems*, pages 4761–4771, 2019.

- Ronen Basri, Meirav Galun, Amnon Geifman, David Jacobs, Yoni Kasten, and Shira Kritchman. Frequency bias in neural networks for input of non-uniform density. In *International Conference on Machine Learning*, pages 685–694. PMLR, 2020.
- Lenaic Chizat, Edouard Oyallon, and Francis Bach. On lazy training in differentiable programming. *arXiv preprint arXiv:1812.07956*, 2018.
- Kamaludin Dingle, Chico Q Camargo, and Ard A Louis. Input–output maps are strongly biased towards simple outputs. *Nature communications*, 9(1):1–7, 2018.
- Simon Du and Wei Hu. Width provably matters in optimization for deep linear neural networks. In *International Conference on Machine Learning*, pages 1655–1664. PMLR, 2019.
- Simon Du, Jason Lee, Haochuan Li, Liwei Wang, and Xiyu Zhai. Gradient descent finds global minima of deep neural networks. In *International Conference on Machine Learning*, pages 1675–1685. PMLR, 2019.
- Simon S Du, Wei Hu, and Jason D Lee. Algorithmic regularization in learning deep homogeneous models: Layers are automatically balanced. *arXiv preprint arXiv:1806.00900*, 2018.
- Kenji Fukumizu. Effect of batch learning in multilayer neural networks. *Gen*, 1(04):1E–03, 1998.
- Gauthier Gidel, Francis Bach, and Simon Lacoste-Julien. Implicit regularization of discrete gradient dynamics in linear neural networks, 2019.
- Daniel Gissin, Shai Shalev-Shwartz, and Amit Daniely. The implicit bias of depth: How incremental learning drives generalization. *arXiv preprint arXiv:1909.12051*, 2019.
- Xavier Glorot and Yoshua Bengio. Understanding the difficulty of training deep feedforward neural networks. In *Proceedings of the thirteenth international conference on artificial intelligence and statistics*, pages 249–256, 2010.
- Suriya Gunasekar, Jason Lee, Daniel Soudry, and Nathan Srebro. Implicit bias of gradient descent on linear convolutional networks. *arXiv preprint arXiv:1806.00468*, 2018.
- Guy Hacoheh, Leshem Choshen, and Daphna Weinshall. Let’s agree to agree: Neural networks share classification order on real datasets. In *International Conference on Machine Learning*, pages 3950–3960. PMLR, 2020.
- Kaiming He, Xiangyu Zhang, Shaoqing Ren, and Jian Sun. Delving deep into rectifiers: Surpassing human-level performance on imagenet classification. In *Proceedings of the IEEE International Conference on Computer Vision (ICCV)*, December 2015.
- Reinhard Heckel and Mahdi Soltanolkotabi. Denoising and regularization via exploiting the structural bias of convolutional generators. *arXiv preprint arXiv:1910.14634*, 2019.
- Wei Hu, Lechao Xiao, Ben Adlam, and Jeffrey Pennington. The surprising simplicity of the early-time learning dynamics of neural networks. *arXiv preprint arXiv:2006.14599*, 2020a.

- Wei Hu, Lechao Xiao, and Jeffrey Pennington. Provable benefit of orthogonal initialization in optimizing deep linear networks. *arXiv preprint arXiv:2001.05992*, 2020b.
- Arthur Jacot, Franck Gabriel, and Clément Hongler. Neural tangent kernel: Convergence and generalization in neural networks, 2020.
- Ziwei Ji and Matus Telgarsky. Gradient descent aligns the layers of deep linear networks. *arXiv preprint arXiv:1810.02032*, 2018.
- Kenji Kawaguchi. Deep learning without poor local minima. *arXiv preprint arXiv:1605.07110*, 2016.
- Alex Krizhevsky, Geoffrey Hinton, et al. Learning multiple layers of features from tiny images. 2009.
- David Krueger, Nicolas Ballas, Stanislaw Jastrzebski, Devansh Arpit, Maxinder S Kanwal, Tegan Maharaj, Emmanuel Bengio, Asja Fischer, and Aaron Courville. Deep nets don't learn via memorization. 2017.
- Thomas Laurent and James Von Brecht. Deep linear neural networks with arbitrary loss: All local minima are global. *arXiv preprint arXiv:1712.01473*, 2017.
- Yann Le Cun, Ido Kanter, and A Sara Solla. Second order properties of error surfaces learning time and generalization. *Advances in neural information processing systems*, 3: 918–924, 1991.
- Mingchen Li, Mahdi Soltanolkotabi, and Samet Oymak. Gradient descent with early stopping is provably robust to label noise for overparameterized neural networks. In *International Conference on Artificial Intelligence and Statistics*, pages 4313–4324. PMLR, 2020.
- Preetum Nakkiran, Gal Kaplun, Dimitris Kalimeris, Tristan Yang, Benjamin L Edelman, Fred Zhang, and Boaz Barak. Sgd on neural networks learns functions of increasing complexity. *arXiv preprint arXiv:1905.11604*, 2019.
- Phan-Minh Nguyen. Analysis of feature learning in weight-tied autoencoders via the mean field lens. *arXiv preprint arXiv:2102.08373*, 2021.
- Iuliia Pliushch, Martin Mundt, Nicolas Lupp, and Visvanathan Ramesh. When deep classifiers agree: Analyzing correlations between learning order and image statistics. *arXiv preprint arXiv:2105.08997*, 2021.
- Nasim Rahaman, Aristide Baratin, Devansh Arpit, Felix Draxler, Min Lin, Fred Hamprecht, Yoshua Bengio, and Aaron Courville. On the spectral bias of neural networks. In *International Conference on Machine Learning*, pages 5301–5310. PMLR, 2019.
- Olga Russakovsky, Jia Deng, Hao Su, Jonathan Krause, Sanjeev Satheesh, Sean Ma, Zhiheng Huang, Andrej Karpathy, Aditya Khosla, Michael Bernstein, et al. Imagenet large scale visual recognition challenge. *International journal of computer vision*, 115(3):211–252, 2015.

- Andrew M Saxe, James L McClelland, and Surya Ganguli. Exact solutions to the nonlinear dynamics of learning in deep linear neural networks. *arXiv preprint arXiv:1312.6120*, 2013.
- Andrew M Saxe, James L McClelland, and Surya Ganguli. A mathematical theory of semantic development in deep neural networks. *Proceedings of the National Academy of Sciences*, 116(23):11537–11546, 2019.
- Harshay Shah, Kaustav Tamuly, Aditi Raghunathan, Prateek Jain, and Praneeth Netrapalli. The pitfalls of simplicity bias in neural networks. *arXiv preprint arXiv:2006.07710*, 2020.
- Eero P Simoncelli and Bruno A Olshausen. Natural image statistics and neural representation. *Annual review of neuroscience*, 24(1):1193–1216, 2001.
- Karen Simonyan and Andrew Zisserman. Very deep convolutional networks for large-scale image recognition. *arXiv preprint arXiv:1409.1556*, 2014.
- Daniel Soudry, Elad Hoffer, Mor Shpigel Nacson, Suriya Gunasekar, and Nathan Srebro. The implicit bias of gradient descent on separable data. *The Journal of Machine Learning Research*, 19(1):2822–2878, 2018.
- Antonio Torralba and Aude Oliva. Statistics of natural image categories. *Network: computation in neural systems*, 14(3):391–412, 2003.
- Dmitry Ulyanov, Andrea Vedaldi, and Victor Lempitsky. Deep image prior. In *Proceedings of the IEEE conference on computer vision and pattern recognition*, pages 9446–9454, 2018.
- Guillermo Valle-Perez, Chico Q Camargo, and Ard A Louis. Deep learning generalizes because the parameter-function map is biased towards simple functions. *arXiv preprint arXiv:1805.08522*, 2018.
- Lei Wu, Qingcan Wang, and Chao Ma. Global convergence of gradient descent for deep linear residual networks. *arXiv preprint arXiv:1911.00645*, 2019a.
- Yifan Wu, Barnabas Poczos, and Aarti Singh. Towards understanding the generalization bias of two layer convolutional linear classifiers with gradient descent. In *The 22nd International Conference on Artificial Intelligence and Statistics*, pages 1070–1078. PMLR, 2019b.
- Gilad Yehudai and Ohad Shamir. On the power and limitations of random features for understanding neural networks. *Advances in Neural Information Processing Systems*, 32: 6598–6608, 2019.
- Chulhee Yun, Shankar Krishnan, and Hossein Mobahi. A unifying view on implicit bias in training linear neural networks. *arXiv preprint arXiv:2010.02501*, 2020.
- Chiyuan Zhang, Samy Bengio, Moritz Hardt, Benjamin Recht, and Oriol Vinyals. Understanding deep learning requires rethinking generalization. *arXiv preprint arXiv:1611.03530*, 2016.
- Yi Zhou and Yingbin Liang. Critical points of linear neural networks: Analytical forms and landscape properties. In *Proc. Sixth International Conference on Learning Representations (ICLR)*, 2018.

Appendix

Appendix A. Random Matrices

A.1 Multiplication of Random Matrices

In this section, we present and prove some statistical properties of general random matrices and their multiplications. Let $\{Q_n \in \mathbb{R}^{m_n \times m_{n-1}}\}_{n=1}^N$ denote a set of random matrix whose elements are sampled iid from a distribution with mean 0 and variance σ_n^2 , with bounded kurtosis. Let

$$\begin{aligned} \mathbf{Q}^l &= \prod_{n=l-1}^1 Q_n = Q_{l-1} \cdots Q_1, & B^l &= \mathbf{Q}^{l\top} \mathbf{Q}^l \in \mathbb{R}^{m_0 \times m_0} \quad l \in [2 \dots N] \\ \mathbf{Q}^l &= \prod_{n=N}^{l+1} Q_n = Q_N \cdots Q_{l+1}, & A^l &= \mathbf{Q}^l \mathbf{Q}^{l\top} \in \mathbb{R}^{m_N \times m_N} \quad l \in [1 \dots N-1] \end{aligned} \quad (6)$$

Theorem 9 $\forall l$

$$\mathbb{E}(B^l) = \beta_l I \quad \beta_l = \prod_{n=1}^{l-1} m_n \sigma_n^2 \quad (7)$$

$$\mathbb{E}(A^l) = \alpha_l I \quad \alpha_l = \prod_{n=l+1}^N m_{n-1} \sigma_n^2 \quad (8)$$

Proof We only prove (7), as the proof of (8) is similar. To simplify the presentation, we use the following auxiliary notations: $V = Q_1$, $U = \prod_{n=l-1}^2 Q_n \implies \mathbf{Q}^l = UV$.

Proof proceeds by induction on l .

- $l = 2$:

$$\begin{aligned} \mathbb{E}[B_{ij}^l] &= \mathbb{E}\left[\sum_{k=1}^{m_1} V_{ki} V_{kj}\right] \stackrel{i \neq j}{=} \sum_{k=1}^{m_1} \mathbb{E}[V_{ki}] \mathbb{E}[V_{kj}] \\ \mathbb{E}[B_{ii}^l] &= \mathbb{E}\left[\sum_{k=1}^{m_1} V_{ki} V_{ki}\right] = \sum_{k=1}^{m_1} \mathbb{E}[V_{ki}^2] \end{aligned}$$

Thus

$$\mathbb{E}[B_{ij}^l] = \begin{cases} 0 & i \neq j \quad (\text{off diagonal}) \\ m_1 \sigma_1^2 & i = j \quad (\text{diagonal}) \end{cases}$$

- Assume that (7) holds for $l-1$.

$$B_{ij}^l = \sum_k \mathbf{Q}_{ki}^l \mathbf{Q}_{kj}^l = \sum_k \sum_{\nu} U_{k\nu} V_{\nu i} \sum_{\rho} U_{k\rho} V_{\rho j}$$

and therefore

$$\mathbb{E}[B_{ij}^l] = \sum_k \sum_{\nu} \sum_{\rho} \mathbb{E}[U_{k\nu} V_{\nu i} U_{k\rho} V_{\rho j}] = \sum_{\nu} \sum_{\rho} \mathbb{E}[V_{\nu i} V_{\rho j}] \sum_k \mathbb{E}[U_{k\nu} U_{k\rho}]$$

where the last transition follows from the independence of U and V . Once again, we consider the diagonal and off-diagonal elements separately. If $i \neq j$:

$$\mathbb{E}[B_{ij}^l] = \sum_{\nu} \sum_{\rho} \mathbb{E}[V_{\nu i}] \mathbb{E}[V_{\rho j}] \sum_k \mathbb{E}[U_{k\nu} U_{k\rho}] = 0$$

If $i = j$:

$$\mathbb{E}[B_{ii}^l] = \sum_{\nu} \sum_{\rho} \mathbb{E}[V_{\nu i} V_{\rho j}] \mathbb{E}[(U^\top U)_{\nu\rho}] = \sum_{\nu} \mathbb{E}[V_{\nu i}^2] \mathbb{E}[(U^\top U)_{\nu\nu}]$$

Using the induction assumption

$$\mathbb{E}[B_{ij}^l] = \begin{cases} 0 & i \neq j \quad (\text{off diagonal}) \\ m_1 \sigma_1^2 \prod_{n=2}^{l-1} m_n \sigma_n^2 & i = j \quad (\text{diagonal}) \end{cases}$$

from which (7) follows. ■

Let \mathfrak{m} denote the width of the smallest hidden layer, $\mathfrak{m} = \min(m_1, \dots, m_{N-1})$, and assume that $\max(m_1, \dots, m_{N-1}) - \min(m_1, \dots, m_{N-1})$ is bounded by some M_b as $\mathfrak{m} \rightarrow \infty$. Assume the following initialization scheme

Definition 10 *The elements of $\{Q_n\}_{n=1}^N$ are chosen iid from a distribution with mean 0 and variance σ_n^2 , where*

$$\sigma_n^2 = \frac{2}{m_{n-1} + m_n} \quad 1 < n < N, \quad \sigma_1^2 = \frac{1}{m_1}, \quad \sigma_N^2 = \frac{1}{m_{N-1}}$$

For large \mathfrak{m} , it follows that

$$\begin{aligned} m_n \sigma_n^2 &= 1 + O\left(\frac{1}{\mathfrak{m}}\right) & n \in [1 \dots N-1] \\ m_{n-1} \sigma_n^2 &= 1 + O\left(\frac{1}{\mathfrak{m}}\right) & n \in [2 \dots N] \end{aligned}$$

Corollary 11 *With initialization as in Def. 10, $\forall l$*

$$\mathbb{E}(B^l) = [1 + O\left(\frac{1}{\mathfrak{m}}\right)]I, \quad \mathbb{E}(A^l) = [1 + O\left(\frac{1}{\mathfrak{m}}\right)]I$$

Theorem 12 *With initialization as in Def. 10, $\forall l$*

$$\text{var}(B^l) = O\left(\frac{1}{\mathfrak{m}}\right), \quad \text{var}(A^l) = O\left(\frac{1}{\mathfrak{m}}\right)$$

Proof

We prove by induction on l that:

$$\mathbb{E}[(B_{ij}^l)^2] = \begin{cases} O\left(\frac{1}{\mathfrak{m}}\right) & i \neq j \quad (\text{off diagonal}) \\ 1 + O\left(\frac{1}{\mathfrak{m}}\right) & i = j \quad (\text{diagonal}) \end{cases}, \quad \mathbb{E}[B_{ii}^l B_{jj}^l] = 1 + O\left(\frac{1}{\mathfrak{m}}\right) \quad (9)$$

For $l = 2$, (9) follows from Lemma 18 and Corr 11. We now assume that (9) holds for $l - 1$ and prove for l , using notations as above: $V = Q_1$, $U = \prod_{l=1}^2 Q_n$, $\mathbf{Q}^l = UV$.

$$\mathbb{E}[(B_{ij}^l)^2] = \sum_{\nu, \rho} \sum_{\alpha, \beta} \mathbb{E}[V_{\nu i} V_{\rho j} V_{\alpha i} V_{\beta j}] \sum_{k, n} U_{k\nu} U_{k\rho} U_{n\alpha} U_{n\beta}$$

Let $B' = U^\top U$. Using the induction assumption

$$\mathbb{E}[(B_{ij}^l)^2] \stackrel{i \neq j}{=} \sum_{\nu, \rho} \mathbb{E}[V_{\nu i}^2 V_{\nu j}^2] \mathbb{E}[(B'_{\nu\rho})^2] = O\left(\frac{1}{\mathfrak{m}}\right)$$

When $i = j$, there are 3 cases where the terms in the sum above do not equal 0: (i) $\nu = \alpha$, $\rho = \beta$, $\nu \neq \rho$ or $\nu = \beta$, $\rho = \alpha$, $\nu \neq \rho$; (ii) $\nu = \rho$, $\alpha = \beta$, $\nu \neq \alpha$; (iii) $\nu = \rho = \alpha = \beta$. Case (i) is similar to the above, and we therefore only expand cases (ii) and (iii) next:

$$\begin{aligned} \text{(ii)} \quad & \sum_{\nu, \alpha} \mathbb{E}[V_{\nu i}^2 V_{\alpha i}^2] \mathbb{E}[B'_{\nu\nu} B'_{\alpha\alpha}] = 1 + O\left(\frac{1}{\mathfrak{m}}\right) \\ \text{(iii)} \quad & \sum_{\nu} \mathbb{E}[V_{\nu i}^4] \mathbb{E}[(B'_{\nu\nu})^2] = O\left(\frac{1}{\mathfrak{m}}\right) \end{aligned}$$

In the derivation of (iii) we exploit the assumption that the kurtosis of the distribution used to sample Q_n is fixed at G and cannot depend on \mathfrak{m} , indicating that $\mathbb{E}[V_{\nu i}^4] = G\sigma_1^4$.

A similar argument would show that $\mathbb{E}[B_{ii}^l B_{jj}^l] = 1 + O\left(\frac{1}{\mathfrak{m}}\right)$. ■

Theorem 13 *Let $\{X(\mathfrak{m})\}$ denote a sequence of random matrices where $\mathbb{E}[X(\mathfrak{m})] = [1 + O\left(\frac{1}{\mathfrak{m}}\right)]I$ and $\text{var}[X(\mathfrak{m})] = O\left(\frac{1}{\mathfrak{m}}\right)$. Then $X(\mathfrak{m}) \xrightarrow{p} I$, where \xrightarrow{p} denotes convergence in probability.*

Proof We need to show that $\forall \epsilon, \delta > 0 \exists \mathfrak{m}' \in \mathbb{N}$, such that $\forall \mathfrak{m} > \mathfrak{m}'$

$$P(|X(\mathfrak{m}) - I| > \epsilon) < \delta$$

Henceforth we use X as shorthand for $X(\mathfrak{m})$. Since $\mathbb{E}(X) = [1 + O\left(\frac{1}{\mathfrak{m}}\right)]I$, it follows that $\forall \epsilon > 0 \exists \mathfrak{m}_1 \in \mathbb{N}$ such that $\forall \mathfrak{m} > \mathfrak{m}_1$, the following holds:

$$|\mathbb{E}(X) - I| < \frac{\epsilon}{2}$$

Thus

$$P(|X - I| > \epsilon) \leq P\left(|X - \mathbb{E}(X)| > \frac{\epsilon}{2}\right)$$

Since $\text{var}(X) = O\left(\frac{1}{m}\right)$, it follows that $\forall \varepsilon, \delta > 0, \exists m_2 \in \mathbb{N} \ni \forall m > m_2$

$$\text{var}(X) < \frac{\varepsilon^2}{4}\delta$$

From the above, and using Chebyshev inequality

$$P(|X - I| > \varepsilon) < \frac{4\text{var}(X)}{\varepsilon^2} < \delta$$

$\forall m > m'$, where $m' = \max\{m_1, m_2\}$. ■

Let $A^l(m)$ and $B^l(m)$ denote a sequence of random matrices as defined in (6), corresponding to models for which $m = \min(m_1, \dots, m_{L-1})$.

Corollary 14

$$B^l(m) \xrightarrow{P} I \quad \forall l \in [2 \dots N] \quad A^l(m) \xrightarrow{P} I \quad \forall l \in [1 \dots N - 1]$$

The proof follows from Cor 11, Thm 12 and Thm 13.

A.2 Dynamics of Random Matrices

Consider a dynamical process, where the random matrices defined above are changed as $Q_j \rightarrow Q_j - \Delta Q_j \forall j$, and specifically from (23):

$$\Delta Q_j = \mu \left(\prod_{n=N}^{j+1} Q_n \right)^\top E_r \left(\prod_{n=j-1}^1 Q_n \right)^\top, \quad E_r = \left(\prod_{n=N}^1 Q_n \right) \Sigma_{XX} - \Sigma_{YX} \quad (10)$$

Denoting $Q^l \rightarrow Q^l - \Delta Q^l$ and applying the product rule

$$\Delta Q^l = \sum_{j=1}^{l-1} \left(\prod_{n=l-1}^{j+1} Q_n \right) \Delta Q_j \left(\prod_{n=j-1}^1 Q_n \right) \quad (11)$$

For $B^l = Q^{l\top} Q^l$ and denoting $B^l \rightarrow B^l - \Delta B^l$:

$$\Delta B^l = [\Delta Q^{l\top} Q^l + Q^{l\top} \Delta Q^l] \quad (12)$$

Before proceeding to analyze ΔB^l , we note that

$$m_N \sigma_N^2 = \frac{K}{m_{N-1}} = \frac{K}{m} \left[1 + O\left(\frac{1}{m}\right) \right]$$

and therefore from Thm 9

$$\mathbb{E}[(Q^{N\top})Q^N] = \left[\frac{K}{m} + O\left(\frac{1}{m}\right) \right] I \quad (13)$$

Theorem 15 For sequence $B^l(m)$ defined as above, if

$$B^l(m) \xrightarrow{p} I, \quad \text{var}[B^l(m)] = O\left(\frac{1}{\mathfrak{m}}\right)$$

then

$$\Delta B^l(m) \xrightarrow{p} 0, \quad \text{var}[\Delta B^l(m)] = O\left(\frac{1}{\mathfrak{m}}\right)$$

Proof

$B^l(m) \xrightarrow{p} I$ implies that $\forall \epsilon, \delta > 0 \exists \hat{\mathfrak{m}} \in \mathbb{N}$, such that $\forall \mathfrak{m} > \hat{\mathfrak{m}}$ and with probability larger than $1 - \delta$.

$$B^l(m) = I + e_1 \quad |e_1| < \epsilon, \quad \forall l \in [2 \dots N] \quad (14)$$

In addition, from (13) and Thms. 12-13

$$Q^{N\top} Q^N = \frac{K}{\mathfrak{m}} I + e_2 \quad |e_2| < \epsilon$$

We fix \mathfrak{m} and let B^l be a shorthand for $B^l(m)$. Now

$$B^{N+1} = \mathbf{Q}_{N-1}^\top Q^{N\top} Q^N \mathbf{Q}_{N-1} = \frac{K}{\mathfrak{m}} \mathbf{Q}^{N-1\top} \mathbf{Q}^{N-1} + O(\epsilon) = \frac{K}{\mathfrak{m}} I + O(\epsilon) \quad (15)$$

To evaluate ΔB^l from (12), we start from

$$\mathbf{Q}^l \top \Delta \mathbf{Q}^l = \sum_{j=1}^{l-1} \left(\prod_{l-1}^1 \mathbf{Q}_n \right)^\top \left(\prod_{l-1}^{j+1} \mathbf{Q}_n \right) \Delta \mathbf{Q}_j \prod_{j-1}^1 \mathbf{Q}_n$$

Simplifying t_j – the j^{th} term in the sum

$$t_j = \mu \prod_1^{l-1} \mathbf{Q}_n^\top \prod_{l-1}^{j+1} \mathbf{Q}_n \prod_{j+1}^N \mathbf{Q}_n^\top E_r \prod_1^{j-1} \mathbf{Q}_n^\top \prod_{j-1}^1 \mathbf{Q}_n = \mu B^l (B^{j+1})^{-1} \mathbf{Q}^{N\top} E_r B^j + O(\epsilon)$$

The last transition is exactly true when $B^l = I$ and $B^{j+1} = I$, as shown in Lemma 19 in §A.3. Substituting E_r

$$\begin{aligned} t_j &= \mu B^l (B^{j+1})^{-1} \mathbf{Q}^{N\top} [\mathbf{Q}^N \Sigma_{XX} - \Sigma_{YX}] B^j + O(\epsilon) \\ &= \mu B^l (B^{j+1})^{-1} [B^{N+1} \Sigma_{XX} + \mathbf{Q}^{N\top} \Sigma_{YX}] B^j + O(\epsilon) \end{aligned}$$

Substituting (14) and (15)

$$t_j = \mu \left[\frac{K}{\mathfrak{m}} \Sigma_{XX} + \mathbf{Q}^{N\top} \Sigma_{YX} \right] + O(\epsilon) \quad (16)$$

From (16) and Lemma 18

$$\mathbb{E}[\mathbf{Q}^l \top \Delta \mathbf{Q}^l] = \sum_{j=1}^{l-1} \mathbb{E}[t_j] = \mu l \frac{K}{\mathfrak{m}} I + O(\epsilon)$$

Since $\Delta \mathbf{Q}^l \top \mathbf{Q}^l = [\mathbf{Q}^{l \top} \Delta \mathbf{Q}^l] \top$, it follows from (12) that

$$\mathbb{E}[\Delta B^l] = 2\mu l \frac{K}{\mathfrak{m}} I + O(\varepsilon) \quad (17)$$

To conclude the proof, we need to show that $\forall \varepsilon', \delta' > 0 \exists \hat{\mathfrak{m}}' \in \mathbb{N}$, such that $\forall \mathfrak{m} > \hat{\mathfrak{m}}'$

$$P\left(|\Delta B^l| > \varepsilon'\right) < \delta'$$

Since (17) is true with probability $(1 - \delta) \forall \varepsilon, \delta$ and $\forall \mathfrak{m} > \hat{\mathfrak{m}}$, we choose ε and $\hat{\mathfrak{m}}'$ such that

$$|\mathbb{E}[\Delta B^l]| < \frac{\varepsilon'}{2} \quad \forall \mathfrak{m} > \hat{\mathfrak{m}}' \quad (18)$$

$$P\left(|\Delta B^l| > \varepsilon'\right) \leq (1 - \delta) P\left(|\Delta B^l - \mathbb{E}(\Delta B^l)| > \frac{\varepsilon'}{2}\right) < \frac{4\text{var}(\Delta B^l)}{\varepsilon'^2} (1 - \delta)$$

$\text{var}(\Delta B^l) = O\left(\frac{1}{\mathfrak{m}}\right)$ implies that $\exists \hat{\mathfrak{m}}'' \in \mathbb{N}, \delta > 0$, such that $\forall \mathfrak{m} > \hat{\mathfrak{m}}''$

$$\frac{4\text{var}(\Delta B^l)}{\varepsilon'^2} (1 - \delta) < \delta'$$

It now follows that $\Delta B^l(m) \xrightarrow{p} 0$.

To analyze the variance, we assume that all the moments of the distribution functions used to sample Q_n are bounded. Thus, from (16), the variance of $t_j \forall j$ remains $O\left(\frac{1}{\mathfrak{m}}\right)$. Likewise, since ΔB^l is a sum of matrices, each with variance $O\left(\frac{1}{\mathfrak{m}}\right)$ thus bounding the covariance by $O\left(\frac{1}{\mathfrak{m}}\right)$, we can deduce that $\text{var}(\Delta B^l) = O\left(\frac{1}{\mathfrak{m}}\right)$. ■

Theorem 16 *For sequence $A^l(m)$ defined as above, if*

$$A^l(m) \xrightarrow{p} I \quad \text{and} \quad \text{var}[A^l(m)] = O\left(\frac{1}{\mathfrak{m}}\right)$$

then

$$\Delta A^l(m) \xrightarrow{p} 0 \quad \text{and} \quad \text{var}[\Delta A^l(m)] = O\left(\frac{1}{\mathfrak{m}}\right)$$

The proof is mostly similar to Thm 15, though we additionally need to show the following in order to replace (13):

$$\mathbb{E}[\mathbf{Q}^0 \Sigma_{xx} \mathbf{Q}^{0 \top}] = \left[\frac{q}{\mathfrak{m}} + O\left(\frac{1}{\mathfrak{m}}\right)\right] I$$

This, in turn, can be proved similarly to the proof of Thm 9, when taking into account the initialization scheme defined in Def. 10.

Note about convergence rate. In Thm 15, convergence to 0 when $\mathfrak{m} \rightarrow \infty$ is governed by $O\left(\frac{K}{\mathfrak{m}}\right)$. In Thm 16, convergence is governed by $O\left(\frac{q}{\mathfrak{m}}\right)$.

A.3 Some Useful Lemmas

Lemma 17 Given function $G(W) = \frac{1}{2}\|UWVX - Y\|_F^2$, its derivative is the following

$$\frac{dG(W)}{dW} = U^\top UWVX(VX)^\top - U^\top Y(VX)^\top = U^\top [UWV\Sigma_{XX} - \Sigma_{YX}]V^\top \quad (19)$$

Lemma 18 Given $\mathbf{Q} = \prod_{n=N}^1 Q_n$, where $Q_n \in \mathbb{R}^{m_n \times m_{n-1}}$ denotes a random matrix whose elements are sampled iid from a distribution with mean 0 and variance σ_n^2 , $\forall i, j$.

$$\mathbb{E}[\mathbf{Q}_{ij}] = 0 \quad \text{var}[\mathbf{Q}_{ij}] = \frac{1}{m_N} \prod_{n=1}^N m_n \sigma_n^2 \quad (20)$$

Proof By induction on N . Clearly for $N = 1$:

$$\mathbb{E}[\mathbf{Q}_{ij}] = \mathbb{E}[(Q_1)_{ij}] = 0 \quad \text{var}[\mathbf{Q}_{ij}] = \text{var}[(Q_1)_{ij}] = \sigma_1^2$$

Assume that (20) holds for $N - 1$. Let $V = \prod_{n=N-1}^1 Q_n$, $U = Q_N$. It follows that

$$\mathbb{E}[\mathbf{Q}_{ij}] = \mathbb{E}[(UV)_{ij}] = \sum_k \mathbb{E}[U_{ik}V_{kj}] = \sum_k \mathbb{E}[U_{ik}]\mathbb{E}[V_{kj}] = 0$$

where the last transition follows from the independence of U and V . In a similar manner

$$\begin{aligned} \text{var}[\mathbf{Q}_{ij}] &= \mathbb{E}[\mathbf{Q}_{ij}^2] = \mathbb{E}\left[\left(\sum_k U_{ik}V_{kj}\right)^2\right] = \mathbb{E}\left[\sum_k U_{ik}V_{kj} \sum_l U_{il}V_{lj}\right] = \sum_k \mathbb{E}[U_{ik}^2]\mathbb{E}[V_{kj}]^2 \\ &= m_{N-1}\sigma_N^2 \frac{1}{m_{N-1}} \prod_{n=1}^{N-1} m_n \cdot \sigma_n^2 = \frac{1}{m_N} \prod_{n=1}^N m_n \cdot \sigma_n^2 \end{aligned}$$

With the initialization scheme defined in Def. 10, $\text{var}(\mathbf{Q}_{ij}) = O\left(\frac{1}{m}\right)$. ■

Lemma 19 Consider matrix multiplication CD where $C \in \mathbb{R}^{k \times m}$, $D \in \mathbb{R}^{m \times k}$, $k \ll m$ and $\text{rank}(CD) = k$. Define $\Delta_1 \in \mathbb{R}^{m \times k}$, $\Delta_2 \in \mathbb{R}^{k \times m}$. Then

$$C\Delta_1 = \Delta_2\Delta_1 = I \implies CD = C\Delta_1\Delta_2D$$

Proof Since $C = \Delta_1^+$ and $\Delta_2 = \Delta_1^+$

$$C = \Delta_1^+\Delta_1C = C\Delta_1\Delta_1^+ = C\Delta_1\Delta_2$$
■

Appendix B. Supplementary Proofs

B.1 Weight Evolution

To analyze the weight dynamics, we first shift to the principal coordinate system defined in Def 1. In this representation $Er^s = W^s D - M$, where $D = \text{diag}(\{d_j\}_{j=1}^q)$ is a diagonal matrix. Based on Prop. 4 and the subsequent discussion of convergence rate, assuming that the width of the hidden layers is very large, we can readily substitute $B_l^s \approx I \forall l$ in (2), to obtain

$$\mathbf{W}^{s+1} = \mathbf{W}^s - \mu \sum_{l=1}^L A_l^s Er^s + O(\mu^2) \quad (21)$$

Let $\mathbf{w}_j \in \mathbb{R}^K$ denote the j -th column of \mathbf{W} , \mathbf{m}_j denote the j -th column of M . From (21) we have

$$\mathbf{w}_j^{s+1} = \mathbf{w}_j^s - \mu \sum_{l=1}^L A_l^s (d_j \mathbf{w}_j^s - \mathbf{m}_j) \quad j \in [K]$$

This is a telescoping series; denoting $A^s = \sum_{l=1}^L A_l^s$,

$$\begin{aligned} \mathbf{w}_j^{s+1} &= \mathbf{w}_j^s - \mu A^s (d_j \mathbf{w}_j^s - \mathbf{m}_j) = (I - \mu d_j A^s) \mathbf{w}_j^s + \mu A^s \mathbf{m}_j = \dots \\ &= \prod_{\nu=1}^s (I - \mu d_j A^\nu) \mathbf{w}_j^0 + \mu \left[\sum_{\nu=1}^s \prod_{\rho=\nu+1}^s (I - \mu d_j A^\rho) A^\nu \right] \mathbf{m}_j \end{aligned} \quad (22)$$

The only difference between individual columns lies in d_j , which governs the rate of convergence of the first term to 0, and the rate of convergence of the second term to the optimal value of $\frac{1}{d_j} \mathbf{m}_j$.

In the discussion following the proof of Thm 5, we noted that the approximation $A_l^s \approx I$ breaks down before $B_l^s \approx I$. Nevertheless, while it is still valid, (22) further simplifies to the following

$$\begin{aligned} \mathbf{w}_j^{s+1} &= (1 - \mu d_j L)^s \mathbf{w}_j^0 + \mu \left[\sum_{\nu=1}^s (1 - \mu d_j L)^{(s-\nu)} L I \right] \mathbf{m}_j = \lambda_j^s \mathbf{w}_j^0 + \mu L \left[\sum_{k=0}^{s-1} \lambda_j^k \right] \mathbf{m}_j \\ &= \lambda_j^s \mathbf{w}_j^0 + (1 - \lambda_j^s) \frac{\mathbf{m}_j}{d_j} \quad \lambda_j = 1 - \mu d_j L \end{aligned}$$

The analysis above is extended to a simple non-linear ReLU model (cf. Arora et al., 2019) as detailed in §3.3, with qualitatively similar results (albeit under unrealistic assumptions). Empirical results, shown in Fig. 2b, indicate that the results are indicative beyond the assumed circumstances.

B.2 Deep Linear networks

Here we prove Prop. 4 as defined in Section 3.1.

Theorem 4. *The compact matrix representation \mathbf{W} obeys the following dynamics*

$$\mathbf{W}^{s+1} = \mathbf{W}^s - \mu \sum_{l=1}^L A_l^s \cdot Er^s \cdot B_l^s + O(\mu^2)$$

where the gradient scale matrices A_l^s , B_l^s are defined in (3)

$$A_l^s := \left(\prod_{j=L}^{l+1} W_j^s \right) \left(\prod_{j=L}^{l+1} W_j^s \right)^\top \in \mathbb{R}^{K \times K} \quad B_l^s := \left(\prod_{j=l-1}^1 W_j^s \right)^\top \left(\prod_{j=l-1}^1 W_j^s \right) \in \mathbb{R}^{q \times q}$$

Proof At time s , the gradient step ΔW_l^s of layer l is defined by differentiating $L(\mathbb{X})$ with respect to W_l^s . Henceforth we omit index s for clarity. First, we rewrite $L(\mathbb{X})$ as follows:

$$L(\mathbb{X}; W_l) = \frac{1}{2} \left\| \left(\prod_{j=L}^{l+1} W_j \right) W_l \left(\prod_{j=l-1}^1 W_j \right) X - Y \right\|_F^2$$

Differentiating $L(\mathbb{X}; W_l)$ to obtain the gradient $\Delta W_l = \frac{\partial L(\mathbb{X}; W_l)}{\partial W_l}$, using Lemma 17 above, we get

$$\Delta W_l = \left(\prod_{j=L}^{l+1} W_j \right)^\top [\mathbf{W} \Sigma_{XX} - \Sigma_{YX}] \left(\prod_{j=l-1}^1 W_j \right)^\top \quad (23)$$

Finally

$$\Delta \mathbf{W} = \prod_{l=L}^1 (W_l - \mu \Delta W_l) - \prod_{l=L}^1 W_l = -\mu \sum_{l=1}^L \left(\prod_{n=L}^{l+1} W_n \right) \Delta W_l \left(\prod_{n=l-1}^1 W_n \right) + O(\mu^2)$$

Substituting ΔW_l and Er (as defined in Def. 3) into the above completes the proof. ■

B.3 Adding Non-Linear ReLU Activation

In this section, we analyze the two-layer model with ReLU activation, where only the weights of the first layer are being learned (Arora et al., 2019). Similarly to (1), the loss is defined as

$$L(\mathbb{X}) = \frac{1}{2} \sum_{i=1}^n \|f(\mathbf{x}_i) - \mathbf{y}_i\|^2 \quad f(\mathbf{x}_i) = \mathbf{a}^\top \cdot \sigma(W \mathbf{x}_i), \quad \mathbf{a} \in \mathbb{R}^m, \quad W \in \mathbb{R}^{m \times d}$$

m denotes the number of neurons in the hidden layer. We consider a binary classification problem with 2 classes, where $y_i = 1$ for $\mathbf{x}_i \in C_1$, and $y_i = -1$ for $\mathbf{x}_i \in C_2$. $\sigma(\cdot)$ denotes the ReLU activation function applied element-wise to vectors, where $\sigma(u) = u$ if $u \geq 0$, and 0 otherwise.

At time s , each gradient step is defined by differentiating $L(\mathbb{X})$ with respect to W . Due to the non-linear nature of the activation function $\sigma(\cdot)$, we separately⁵ differentiate each row of W , denoted \mathbf{w}_r where $r \in [m]$, as follows:

5. Since the ReLU function is not everywhere differentiable, the following may be considered the definition of the update rule.

$$\begin{aligned}
 \mathbf{w}_r^{s+1} - \mathbf{w}_r^s &= -\mu \frac{\partial L(\mathbb{X})}{\partial \mathbf{w}_r} \Big|_{\mathbf{w}_r = \mathbf{w}_r^s} = -\mu \sum_{i=1}^n \left[\mathbf{a}^\top \cdot \sigma(W^s \mathbf{x}_i) - y_i \right] \frac{\partial f(\mathbf{x}_i)}{\partial \mathbf{w}_r} \Big|_{\mathbf{w}_r = \mathbf{w}_r^s} \\
 &= -\mu \sum_{i=1}^n \left[\sum_{j=1}^m a_j \sigma(\mathbf{w}_j^s \cdot \mathbf{x}_i) - y_i \right] a_r \mathbf{x}_i^\top \mathbb{1}_{\mathbf{w}_r^s}(\mathbf{x}_i) \\
 &= -\mu a_r \sum_{i=1}^n \mathbb{1}_{\mathbf{w}_r^s}(\mathbf{x}_i) \left[\Psi^s(\mathbf{x}_i) \cdot \mathbf{x}_i - y_i \right] \mathbf{x}_i^\top \quad \text{where } \Psi^s(\mathbf{x}_i) = \sum_{j=1}^m a_j \mathbf{w}_j^s \mathbb{1}_{\mathbf{w}_j^s}(\mathbf{x}_i)
 \end{aligned}$$

Above $\mathbb{1}_{\mathbf{w}_r^s}(\mathbf{x}_i)$ denotes the indicator function that equals 1 when $\mathbf{w}_r^s \cdot \mathbf{x}_i \geq 0$, and 0 otherwise.

In order to proceed, we make two assumptions:

1. The distribution of the data is symmetric where $P(\mathbf{x}_i) = P(-\mathbf{x}_i)$.
2. W and \mathbf{a} are initialized so that $\mathbf{w}_{2i}^0 = -\mathbf{w}_{2i-1}^0$ and $a_{2i} = -a_{2i-1} \quad \forall i \in [\frac{m}{2}]$.

It follows from Assumption 2 that at the beginning of training $\mathbb{1}_{\mathbf{w}_{2j}^0}(\mathbf{x}_i) + \mathbb{1}_{\mathbf{w}_{2j-1}^0}(\mathbf{x}_i) = 1$, $\forall \mathbf{x}_i$ such that $\mathbf{w}_{2j-1}^0 \mathbf{x}_i \neq \mathbf{w}_{2j}^0 \mathbf{x}_i \neq 0$, and $\forall j \in [\frac{m}{2}]$. Consequently

$$\Psi^0(\mathbf{x}_i) = \sum_{j=1}^m a_j \mathbf{w}_j^0 \mathbb{1}_{\mathbf{w}_j^0}(\mathbf{x}_i) = \frac{1}{2} \sum_{j=1}^m a_j \mathbf{w}_j^0 = \frac{1}{2} \mathbf{a}^\top W^0$$

$\forall \mathbf{x}_i$ such that $\mathbf{w}_{2j-1}^0 \mathbf{x}_i \neq \mathbf{w}_{2j}^0 \mathbf{x}_i \neq 0$. Finally

$$\mathbf{w}_r^1 - \mathbf{w}_r^0 = -\mu a_r \left[\frac{1}{2} \mathbf{a}^\top W^0 \sum_{\substack{i=1 \\ \mathbf{w}_r^0 \mathbf{x}_i \geq 0}}^n \mathbf{x}_i \mathbf{x}_i^\top - \sum_{\substack{i=1 \\ \mathbf{w}_r^0 \mathbf{x}_i \geq 0}}^n y_i \mathbf{x}_i^\top \right]$$

Next, we note that Assumption 1 implies

$$\mathbb{E} \left[\sum_{\substack{i=1 \\ \mathbf{w} \cdot \mathbf{x}_i \geq 0}}^n \mathbf{x}_i \mathbf{x}_i^\top \right] = \frac{1}{2} \mathbb{E} \left[\sum_{i=1}^n \mathbf{x}_i \mathbf{x}_i^\top \right] = \frac{1}{2} \mathbb{E}[\Sigma_{XX}]$$

for any vector \mathbf{w} . Thus, if the sample size n is large enough, at the beginning of training we expect to see

$$\mathbf{w}_r^{s+1} - \mathbf{w}_r^s \approx -\mu \frac{a_r}{2} [\mathbf{a}^\top W^s \Sigma_{XX} - \tilde{\mathbf{m}}_r^s] \quad \forall r$$

where row vector $\tilde{\mathbf{m}}_r^s$ denotes the vector difference between the centroids of classes C_1 and C_2 , computed in the half-space defined by $\mathbf{w}_r^s \cdot \mathbf{x} \geq 0$. Finally (for small s)

$$W^{s+1} - W^s \approx -\mu \frac{1}{2} \left[(\mathbf{a} \mathbf{a}^\top) W^s \Sigma_{XX} - \tilde{M}^s \right]$$

where \tilde{M}^s denotes the matrix whose r -th row is $a_r \tilde{\mathbf{m}}_r^s$. This equation is reminiscent of the single-layer linear model dynamics $\mathbf{W}^{s+1} = \mathbf{W}^s - \mu E r^s$, and we may conclude that when it holds and using the principal coordinate system, the rate of convergence of the j -th column of W^s is governed by the singular value d_j .

Appendix C. Additional Empirical Results

C.1 Weight Initialization

We evaluate empirically the weight initialization scheme from Def. 10. When compared to Glorot uniform initialization (Glorot and Bengio, 2010), the only difference between the two schemes lies in how the first and last layers are scaled. Thus, to highlight the difference between the methods, we analyze a fully connected linear network with a single hidden layer, whose dimension (the number of hidden neurons) is much larger than the input and output dimensions. We trained $N=10$ such networks on a binary classification problem, once with the initialization suggested in Def. 10, and again with Glorot uniform initialization. While both initialization schemes achieve the same final accuracy upon convergence, our proposed initialization variant converges faster on both train and test datasets (see Fig. 11).

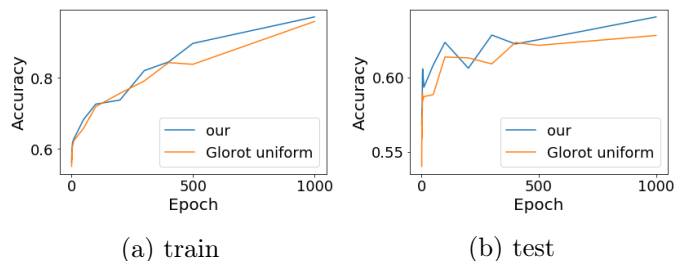


Figure 11: Learning curves of a fully connected linear network with one hidden layer, trained on the dogs and cats dataset, and initialized by Glorot uniform initialization (orange) and the initialization proposed in Def. 10 (blue).

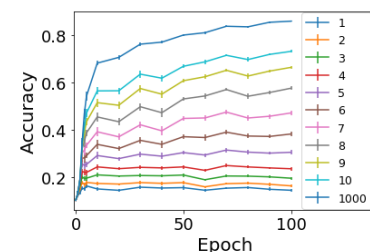


Figure 12: Evaluations on test-sets projected to the first P principal components, for different values of P (see legend) of 10 VGG-19 models trained on CIFAR-10

C.2 Spectral Bias

The *spectral bias*, discussed in Section 5.3, can also induce similar learning order in different networks. To support the discussion in Section 5.3, in §C.2.2) we analyze the relation between the *spectral bias* and *accessibility*, in order to clarify its relation to the *Learning Order Constancy* and the *PC-bias*. First, however, we expand the scope of the empirical evidence for this effect to the classification scenario and real image data (§C.2.1).

C.2.1 SPECTRAL BIAS IN CLASSIFICATION

Rahaman et al. (2019) showed that when regressing a 2D function by a neural network, the model seems to approximate the lower frequencies of the function before its higher frequencies. Here we extend this empirical observation to the classification framework. Thus, given frequencies $\kappa = (\kappa_1, \kappa_2, \dots, \kappa_m)$ with corresponding phases $\phi = (\varphi_1, \varphi_2, \dots, \varphi_m)$, we consider the mapping $\lambda : [-1, 1] \rightarrow \mathbb{R}$ given by

$$\lambda(z) = \sum_{i=1}^m \sin(2\pi\kappa_i z + \varphi_i) := \sum_{i=1}^m \text{freq}_i(z) \quad (24)$$

Above κ is strictly monotonically increasing, while ϕ is sampled uniformly.

The classification rule is defined by $\lambda(z) \leq 0$. We created a binary dataset whose points are fully separated by $\lambda(z)$, henceforth called the *frequency dataset* (see the visualization in Fig. 14 and details in §D.4). When training on this dataset, we observe that the frequency of the corresponding separator increases as learning proceeds, in agreement with the results of Rahaman et al. (2019).

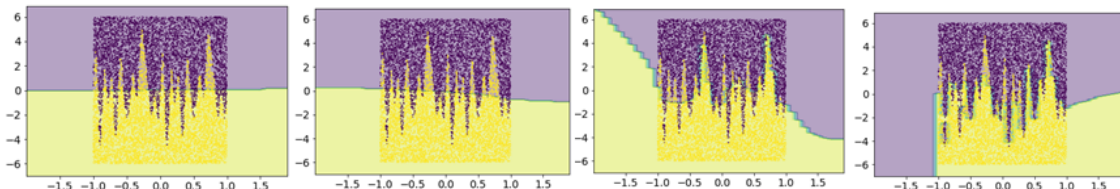


Figure 13: Visualization of the separator learned by st-VGG when trained on the frequency dataset, as captured in advancing epochs (from left to right): 1, 100, 1000, 10000. Each point represents a training example (yellow for one class and purple for the other). The background color represents the classification that the network predicts for points in that region.

To visualize the decision boundary of an st-VGG network trained on this dataset as it evolves with time, we trained $N=100$ st-VGG networks. Since the data lies in \mathbb{R}^2 , we can visualize it and the corresponding network’s inter-class boundary at each epoch as shown in Fig. 13. We can see that the decision boundary incorporates low frequencies at the beginning of the learning, adding the higher frequencies only later on. The same qualitative results are achieved with other instances of st-VGG as well. We note that while the decision functions are very similar in the region where the training data is, at points outside of the data they differ drastically across networks.

C.2.2 SPECTRAL BIAS: RELATION TO ACCESSIBILITY

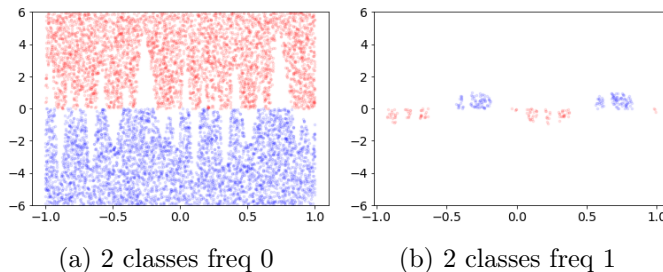
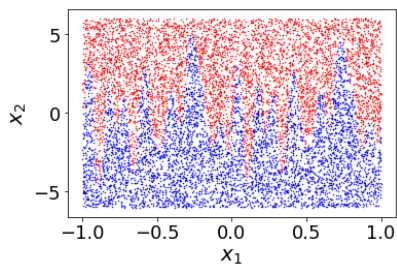


Figure 14: Visualization of the classification dataset used to extend Rahaman et al. (2019) to a classification framework.

Figure 15: Visualization of the *critical frequency*, showing all the points in the 2D-frequency dataset with *critical frequency* of (a) 0, and (b) 1.

To connect between the learning order, which is defined over examples, and the Fourier analysis of a separator, we define for each example its *critical frequency*, which characterizes

the smallest number of frequencies needed to correctly classify the example. To illustrate, consider the *frequency dataset* defined above. Here, the *critical frequency* is defined as the smallest $j \in [m]$ such that $\lambda_j(z) = \sum_{i=1}^j \text{freq}_i(z)$ classifies the example correctly (see Figs. 15a,15b).

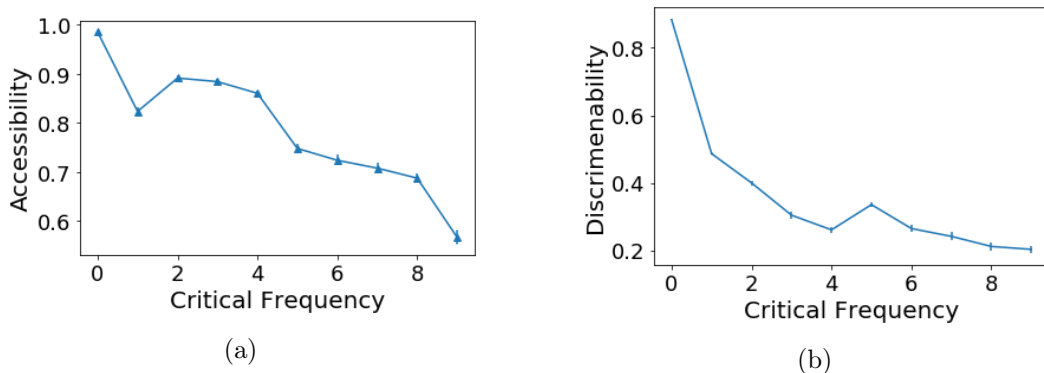


Figure 16: (a) Correlation between *critical frequency* and *accessibility* score in the 2D-frequency dataset. (b) Correlation between *discriminability* and *critical frequency* in the 2D-frequency dataset.

In this binary classification task, we observe a strong connection between the order of learning and the *critical frequency*. Specifically, we trained $N=100$ st-VGG networks on the *frequency dataset*, and correlated the *accessibility* scores with the *critical frequency* of the examples (see Fig. 16a). We see a strong negative correlation ($r = -0.93$, $p < 10^{-2}$), suggesting that examples whose *critical frequency* is high are learned last by the networks.

To see the effect of the *spectral bias* in real classification tasks and extend the above analysis to natural images, we need to define a score that captures the notion of *critical frequency*. To this end, we define the *discriminability* measure of an example - the percentage out of its k neighbors that share the same class as the example. Intuitively, an example has a low *discriminability* score when it is surrounded by examples from other classes, which forces the learned boundary to incorporate high frequencies. In Fig. 16b we plot the correlation between the *discriminability* and the *critical frequency* for the 2D frequency dataset. The high correlation ($r=-0.8$, $p < 10^{-2}$) indicates that *discriminability* indeed captures the notion of *critical frequency*.

C.3 Projection to higher PC's

In Section 4.3 we described an evaluation methodology, based on the creation of a modified *test-set* by projecting each test example on the span of the first P principal components. We repeat this experiment with VGG-19 networks on CIFAR-10, and plot the results in Fig. 12.

Appendix D. Methodology

D.1 Implementation details and hyperparameters

The results reported in Section 6 represent the mean performance of 100 st-VGG and linear st-VGG networks, trained on the small mammals dataset. The results reported in Section 6 represent the mean performance of 10 2-layers fully connected linear networks trained over the cats and dogs dataset. The results in Fig. 10 represent the mean performance of 100 st-VGG network trained on the small mammals dataset. In every experimental setup the network’s hyper-parameters were coarsely grid-searched to achieve good performance over the validation set, for a fair comparison. Other hyper-parameters exhibit similar results.

D.2 Generalization Gap

In Section 6 we discuss the evaluation of networks on datasets with amplified principal components. Examples of these images are shown in Fig. 7: the top row shows examples of the original images, the middle row shows what happens to each image when its 1.5% most significant principal components are amplified, and the bottom row shows what happens when its 1.5% least significant principal components are amplified. Amplification was done by a factor of 10, which is significantly smaller than the ratio between the values of the first and last principal components of the data. After amplification, all the images were re-normalized to have 0 mean and std 1 in every channel as customary.

D.3 Architectures

st-VGG. A stripped version of VGG which we used in many of the experiments. It is a convolutional neural network, containing 8 convolutional layers with 32, 32, 64, 64, 128, 128, 256, 256 filters respectively. The first 6 layers have filters of size 3×3 , and the last 2 layers have filters of size 2×2 . Every other layer is followed by a 2×2 max-pooling layer and a 0.25 dropout layer. After the convolutional layers, the units are flattened, and there is a fully connected layer with 512 units followed by a 0.5 dropout. The batch size we used was 100. The output layer is a fully connected layer with output units matching the number of classes in the dataset, followed by a softmax layer. We trained the network using the SGD optimizer, with cross-entropy loss. When training st-VGG, we used a learning rate of 0.05.

Linear st-VGG. A linear version of the st-VGG network. In linear st-VGG, we change the activation function to the identity function, and replace max-pooling by average pooling with a similar stride.

Linear fully connected network. An L -layered fully connected network. Each layer contains 1024 weights, initialized with Glorot uniform initialization. 0.5 dropout is used before the output layer. Networks are trained with an SGD optimizer, without momentum or L_2 regularization.

D.4 Datasets

In all the experiments and all the datasets, the data was always normalized to have 0 mean and std 1, in each channel separately.

Small Mammals. The small-mammals dataset used in our experiments is the relevant super-class of the CIFAR-100 dataset. It contains 2500 train images divided into 5 classes equally, and 500 test images. Each image is of size $32 \times 32 \times 3$. This dataset was chosen due to its small size.

Cats and Dogs. The cats and dogs dataset is a subset of CIFAR-10. It uses only the 2 relevant classes, to create a binary problem. Each image is of size $32 \times 32 \times 3$. The dataset is divided to 20000 train images (10000 per class) and 2000 test images (1000 per class). This dataset is used when a binary problem is required.

ImageNet-20. The ImageNet-20 dataset is a subset of ImageNet containing 20 classes. This data resembles ImageNet in terms of image resolution and data variability, but contains a smaller number of examples to reduce computation time. The dataset contains 26000 train images (1300 per class) and 1000 test images (50 per class). The choice of the 20 classes was arbitrary, and contained the following classes: boa constrictor, jellyfish, American lobster, little blue heron, Shih-Tzu, scotch terrier, Chesapeake Bay retriever, komondor, snow leopard, tiger, long-horned beetle, warthog, cab, holster, remote control, toilet seat, pretzel, fig, burrito and toilet tissue.

Frequency dataset A binary 2D dataset, used in Section 5.3, to examine the effects of spectral bias in classification. The data is define by the mapping $\lambda : [-1, 1] \rightarrow \mathbb{R}$ given in (24) by

$$\lambda(z) = \sum_{i=1}^m \sin(2\pi\kappa_i z + \varphi_i) := \sum_{i=1}^m \text{freq}_i(z)$$

with frequencies $\kappa = (\kappa_1, \kappa_2, \dots, \kappa_m)$ and corresponding phases $\phi = (\varphi_1, \varphi_2, \dots, \varphi_m)$. The classification rule is defined by $\lambda(z) \leq 0$.

In our experiments, we chose $m = 10$, with frequencies $\kappa_1 = 0, \kappa_2 = 1, \kappa_3 = 2, \dots, \kappa_{10} = 9$. Other choices of m yielded similar qualitative results. The phases were chosen randomly between 0 and 2π , and were set to be: $\varphi_1 = 0, \varphi_2 = 3.46, \varphi_3 = 5.08, \varphi_4 = 0.45, \varphi_5 = 2.10, \varphi_6 = 1.4, \varphi_7 = 5.36, \varphi_8 = 0.85, \varphi_9 = 5.9, \varphi_{10} = 5.16$. As the first frequency is $\kappa_1 = 0$, the choice of φ_0 does not matter, and is set to 0. The dataset contained 10000 training points, and 1000 test points, all uniformly distributed in the first dimension between -1 and 1 and in the second dimension between -2π and 2π . The labels were set to be either 0 or 1, in order to achieve perfect separation with the classification rule $\lambda(z)$.